EUROPEAN ORGANIZATION FOR NUCLEAR RESEARCH

CERN-EP/90-37
23 March 1990

CERN-LAA-HC-90-004

# Results of Prototype Studies for a Spaghetti Calorimeter

D. Acosta[1)], S. Buontempo[2)], L. Calôba[3)], M. Caria[4)], R. DeSalvo[5)], A. Ereditato[2)], R. Ferrari[6)], M. Fraternali[7)], G. Fumagalli[6)], O. Gildemeister[5)], F.G. Hartjes[8)], Th. H. Henkes[9)], A. Henriques[5,10)], L. Linssen[5)], M. Livan[4)], A. Maio[10)], L. Mapelli[5)], K.H. Meier[5)], B. Ong[1)], H.P. Paar[1)], F. Pastore[6)], M. Pereira[10)], L. Poggioli[11)], C.V. Scheel[5,8)], J.M. Seixas[3)], A. Simon[12)], M. Sivertz[1)], P. Sonderegger[5)], M.N. Souza[3)], Z.D. Thomé[3)], V. Vercesi[5)] and R. Wigmans[5,8)]

*1) University of California, San Diego, USA*
*2) Università di Napoli and INFN Sez. Napoli, Italy*
*3) COPPE/EE/UFRJ, Rio de Janeiro, Brazil*
*4) Università di Cagliari and INFN Sez. Cagliari, Italy*
*5) CERN, Geneva, Switzerland*
*6) Università di Pavia and INFN Sez. Pavia, Italy*
*7) Università di Palermo and INFN Sez. Pavia, Italy*
*8) NIKHEF-H, Amsterdam, The Netherlands*
*9) Max Planck Institut, Heidelberg, Germany*
*10) LIP, Lisbon, Portugal*
*11) LPNHE, Université Paris VI, Paris, France*
*12) Universität Heidelberg, Germany*

## Abstract

In the framework of the LAA project, prototypes for a new type of calorimeter, intended for the detection of both electromagnetic and hadronic showers, muons and missing energy (e.g. neutrinos) at high-luminosity multi-TeV $pp$ colliders, were tested. The detector consists of scintillating plastic fibres embedded in a lead matrix at a volume ratio 1:4, such as to achieve compensation. The optimization of the construction of the detector modules is described, as well as the performance concerning e.m. shower and muon detection and $e/\pi$ separation. We used electron, pion and muon beams in the energy range 10-150 GeV for this purpose.

For the energy resolution of electrons we found $13\%/\sqrt{E}$, with a constant term of 1%. The signal uniformity was better than 3% over the total surface of projective modules. The signal linearity for e.m. shower detection was better than 1%, and the $e/\pi$ separation was better than $5.10^{-4}$ for isolated particles. Channeling effects are negligible, provided that the angle between the incoming particles and the fibre axis is larger than $2^0$.



(Submitted to Nuclear Instruments and Methods in Physics Research)

## 1. INTRODUCTION

In the framework of the LAA project, a detector R&D project set up to develop detector technology that may allow meaningful experiments at future high-luminosity multi-TeV $pp$ colliders, we are developing a new type of calorimeter intended for detection of both electromagnetic (e.m.) and hadronic particle showers, muons and missing energy (e.g. neutrinos).

The detector, based on large numbers of scintillating plastic fibres embedded in a lead matrix, is called the Spaghetti Calorimeter (SPACAL). The chosen technique is expected to provide important advantages compared to the currently used calorimeter techniques, advantages that may turn out to be of crucial importance in the Supercollider era. These are mentioned in sect. 2. The rest of this paper is devoted to prototype studies that were performed in the past year and a half.

The detectors were tested with electron, pion and muon beams in the energy range 10-150 GeV. The main emphasis was on the electromagnetic performance (energy resolution, signal linearity, uniformity). Moreover, some results on the $e/\pi$ separation capability and muon detection were obtained. The tests did not yet include the detailed performance concerning hadronic shower detection. The detectors constructed up to now were not large enough to contain such showers at a level sufficient for obtaining meaningful results.

In sect. 3, the construction of the detector modules is described. Results of test beam measurements are presented in sect. 4 and discussed in the concluding sect. 5.

## 2. LEAD-SCINTILLATING FIBRE CALORIMETRY

For a long time, it was thought that the best possible hadron calorimetry requires the use of depleted uranium ($^{238}$U) as absorber material. Several experiments (HELIOS[1] ,D0[2] , ZEUS[3] , L3[4] and UA1[5] ) have built or are building large uranium calorimeters. Two arguments are frequently used to justify this choice. Firstly, because of its high density, uranium allows the construction of very compact detectors. And secondly, the calorimeters may be made *compensating* in this way, which is crucial for the hadronic performance. However, neither of these arguments make uranium a unique option. Calorimeters using other absorber materials, and in particular lead, may yield equally good or better performance concerning the two mentioned points. Moreover, lead absorber offers some crucial advantages compared to uranium.

It is now well known that compensation ($e/h = 1$, i.e. the calorimeter gives on

average equal response to the e.m. and non-e.m. components of hadron showers) is *not* a unique property of $^{238}$U absorber, nor does the use of this material *guarantee* compensation[6] . In fact, a variety of absorber/readout combinations can be made compensating, provided that the response to the neutron shower component is adequately amplified with respect to the charged shower components. This may be achieved with hydrogenous active material.

It was predicted theoretically[7] , and confirmed experimentally[8] , that a lead/plastic-scintillator sampling calorimeter can be made compensating if the passive and active calorimeter components are used in a volume ratio 4:1. This condition implies that the *effective* nuclear interaction length of such a calorimeter is about 20 cm, i.e. equally long as for compensating uranium/scintillator detectors, which need a much larger fraction of low-density plastic scintillator (optimal ratio 1:1)[9] . In other words, *compensating* lead/scintillators and *compensating* uranium/scintillator calorimeters are equally compact.

Another remarkable experimental finding concerns the fact that the hadronic energy resolutions achievable with compensating lead/scintillator calorimeters are *better* than for compensating uranium/scintillator calorimeters. Measurements by the ZEUS Collaboration indicate an intrinsic limit to the hadronic energy resolution of $11\%/\sqrt{E}$ for lead, vs. $19\%/\sqrt{E}$ for uranium[10] .

Apart from the obvious advantages of using lead as absorber material (it is easy to machine, cheap, abundantly available and non-radioactive), we mention two points which are particularly relevant for applications at high-luminosity machines. The first one concerns the *time structure* of the calorimeter signals. In compensated plastic-scintillator calorimeters, a considerable fraction of the signal comes from neutrons produced in the shower development. These neutrons, most of which are generated with kinetic energies of the order of 1 MeV, may contribute to the calorimeter signal in two ways[7] :

*a*) Through processes in which they lose their *kinetic* energy, the most important one being elastic scattering off hydrogen nuclei in the plastic.

*b*) Through capture by an atomic nucleus, in which nuclear binding energy is released as few-MeV $\gamma$'s.

The first process occurs on a time scale of 10 ns, whereas the second takes typically 1 $\mu$s, since its cross section becomes only considerable at thermal energies[11] . The contribution of the latter process to the signal of lead calorimeters is practically absent, in contrast to uranium. The cross section is only 0.1b (compared to 2.7b for $^{238}$U) which corresponds to a mean free path of several meters. Therefore, the signals of compensating lead/scintillator calorimeters are much faster than for uranium: they don't exhibit microsecond tails[12] .

The second point concerns radiation damage. Several studies have shown that neutron-induced damage of electronics is among the most serious problems for doing experiments at the SSC[13] . Hadronic shower development in the calorimeter is *the* source of these neutrons. Because of the absence of nuclear fission, the neutron production in lead calorimeters is about a factor of 3 lower than in depleted uranium[14] .

Summarizing this discussion, we conclude that compensating lead calorimeters, compared to uranium, are as compact, can deliver a better energy resolution, give faster signals and cause less radiation damage.

Having given the arguments why we have chosen lead as absorber material, we now come to the reasons for using scintillating fibres. This choice has nothing to do with the excellent position resolution that can be achieved with these fibres, which has made them popular in tracking devices. The submillimetric precision that can be obtained with fibres is largely irrelevant for shower detection because of the lateral shower dimensions, which amount to at least several centimetres. On the other hand, the arbitrarily fine calorimeter segmentation achievable with fibres is a valuable feature, which eliminates some of the problems encountered in the classical structures with wavelength shifter (WLS) readout.

The original reason for considering fibres was the very frequent shower sampling that they permit to achieve, thus minimizing the contribution of sampling fluctuations to the energy resolution. For compensating lead/scintillator calorimeters, reducing these fluctuations is very relevant, since the contribution of *other* factors (i.e. a constant term and intrinsic fluctuations) is very small, so that the sampling frequency tends to dominate the energy resolution. Based on measurements of the contribution of intrinsic and sampling fluctuations to the energy resolution of a more crudely sampling lead/scintillator calorimeter[10] one may expect resolutions of $13\%/\sqrt{E}$ and $25-30\%/\sqrt{E}$ for detection of electrons and jets, respectively, in a compensating lead calorimeter using 1 mm fibres as active material (fig. 1). In sect. 4 we will show that this expectation is experimentally confirmed for electromagnetic showers.

The fibre technique offers, in addition to what was stated above, some additional major advantages, that are crucial for applications at high-luminosity colliders. We mention three:

*i*) Thanks to the absence of external wavelength shifters, the fibre signals may be extremely fast: rise times of less than 1 ns and fall times below 2 ns have been measured[15] . The total duration of realistic shower signals from hadron calorimeters may be as short as 20 ns, comparable to the bunch spacing of the proposed multi-TeV *pp* colliders. In a recent paper[12] we showed that, thanks to these extremely fast time characteristics, electrons

and pions can be distinguished because of subtle differences occurring in the *time structure* of the signals from e.m. and hadronic showers. We will come back to this point in sect. 4.

*ii*) The use of fibres makes it possible to construct an essentially perfectly *hermetic* calorimeter. In order to achieve this goal, it is necessary that the fibres are oriented longitudinally, i.e. they are running (approximately, in order to avoid channeling, see sect. 4) in the direction of the particles to be detected. This technique has the additional advantage that all the readout elements (light detectors) are located at the downstream end of the detector and, therefore, are easily accessible.

*iii*) The use of fibres has advantages concerning the calibration and gain monitoring, probably one of the most difficult problems to be solved in commissioning and operating a very large detector system based on light as the source of information[16] . It is of crucial importance that the whole optical chain can be tested regularly: the production of scintillation light, the light transmission, the optical coupling between the components, the stability of the readout device and the ADC. The fibre detector offers the possibility to insert radioactive wires in the same way as the fibres. All the active elements (the fibres) are accessible by $\gamma$'s from a radioactive source in this way.

## 3. THE CONSTRUCTION OF THE DETECTOR MODULES.

### *3.1 The mechanics of the SPACAL modules*

For the tests described in this paper, we have constructed in total 16 modules. All modules used fibres with 1 mm diameter and lead absorber and had a hexagonal shape. The lead-to-fibre volume ratio was 4:1 (see sect. 2). This made the detector extremely compact, with an effective radiation length of 7.5 mm, and a nuclear interaction length of 21 cm.

The fibres are arranged in such a way that each one of them is at equal distance from its (6) neighbours (fig. 2a). The lateral size of the hexagonal modules, i.e. the granularity of the detector, was determined by many considerations, such as the typical lateral dimensions of e.m. and hadronic showers, and the segmentation requirements for a calorimeter at a supercollider. Also, the useful surface of standard photomultiplier (PM) photocathodes, the weight of the modules and the possibility of calibrating them with a radioactive $^{60}$Co source replacing one

of the fibres were important criteria. It should be stressed that the lateral granularity can be freely chosen for this type of detector, since one can connect any number of fibres to one readout element.

We finally chose a design that contains 1141 fibres and has a lateral cross section of 48.7 $cm^2$ (86 mm apex-to-apex). For specific e.m. shower studies some of the modules were made smaller, containing 397 fibres (51 mm apex-to-apex). The longitudinal dimensions depended on the intended purpose (e.m. or hadronic shower detection). Electromagnetic modules were made with a length between 24 and $28X_0$; hadronic modules were either 7.5 or $9.5\lambda_{int}$ deep.

For the construction of the modules, three different techniques were used. In one technique, the modules were built using a method in which liquid lead, or rather an alloy that contained a small fraction of antimony for improving the mechanical properties, was cast around very thin stainless steel tubes ($50\mu$m wall thickness). The tubes were held together by spacers, in a matrix corresponding to the desired fibre positions. After casting, the module ends were machined, and the fibres were inserted in the tubes.

In the other two techniques, the modules were constructed from grooved layers of lead plates, produced either by extrusion or by machining.

The extruded plates were tinned and soldered together, producing a lead structure with many parallel channels into which the fibres were inserted later, as in the previously mentioned technique. Both methods have the major advantage that the use of glue can be completely avoided, which makes it easy and fast to replace the fibres if one wants to do so. Moreover, systematic or aging effects that may be due to the glue are absent.

In another technique, only used for producing small e.m. modules, the machined lead plates were epoxied together, with the fibres already in place. This is the method by which other groups built e.m. calorimeters of this type[17] .

The fibres were $\sim$ 15 cm longer than the lead structures. The parts that were sticking out at the back end of the modules were bundled together, machined, polished and coupled to a PM via a plexiglass light guide, avoiding direct optical contacts (fig. 3).

### *3.2 The optics*

The quality of the optics determines to a large extent the quality of the calorimetry achievable with this type of detector. The final design of our detector was the result of several iterations of improvements. The crucial issues are:

*i*) The attenuation length of the fibres.

*ii*) The fibre-to-fibre response fluctuations.

*iii*) The coupling to the PM.

*iv*) The uniformity of the photocathode response.

### *3.2.1 The fibres*

In a previous paper[15] , the requirements on the performance of the fibres for this type of detector were already discussed. These requirements concern:

*i*) The mechanical tolerances on the fibre diameter, because of the way the modules are constructed: $\phi = 1.0$ mm $\pm$ 2%.

*ii*) The attenuation length. In order to limit the contribution of fluctuations in the starting point of the (hadronic) shower on the energy resolution to 1%, $\lambda_{att}$ should be larger than 6 m for single hadrons, and at least 3 m for jet detection.

*iii*) The fibre-to-fibre fluctuations in the response at 2 m from the PM, which should be smaller than 6% in order to limit the contribution of systematic effects to the e.m. energy resolution to 1%.

*iv*) Mechanical properties like robustness, polishability, etc.

These requirements were met by the fibres named SCSN-38, produced by Kyowa Gas Inc. (Japan), which were selected for our detector. They consist of a polystyrene core surrounded by a 29$\mu$m thick acrylic cladding, and emit in the blue region, with a maximum around 420 nm. The required attenuation length could be achieved with a filter, absorbing the light with $\lambda < 450$ nm (which is most strongly attenuated), and by equipping the open front end of the fibre with a high quality mirror. For individual fibres, the required attenuation length could be largely exceeded in this way. For entire modules, this was more difficult to achieve.

This is illustrated in fig. 4, which shows the effect of filter and mirror on the light attenuation curve for a 2 m long module. The module was exposed to a collimated $^{60}$Co ring source surrounding it. The beneficial effects of filter and mirror are obvious. By sacrificing (with the filter) about half of the light, a considerable improvement in the longitudinal uniformity of the response is obtained. The *average* effective attenuation length of the 1141 fibres in the module amounted to 5.1 m. The actual light attenuation curves are not exactly exponential because of, among other reasons, the use of a mirror. The effective attenuation length is defined as the result obtained from an exponential fit to the points in the first metre of the detector, a region where the showers produce in practice more than 95% of their light, on average.

As can be seen from fig. 4, the effective reflection coefficient achieved with the mirror, an aluminized glass plate covering the whole detector surface, was only $\sim 40\%$. This is not due to a poor quality of the mirror surface, but rather to the fact that it was difficult to bring simultaneously a large number of fibres in sufficiently close contact with it. Because of the small fibre diameter and the large index of refraction (1.59), air gaps as small as 0.1 mm are already intolerable. The 40% reflection is therefore rather a measurement of the flatness of the calorimeter front face than of anything else.

This is a very undesirable situation. Firstly, an increase of the effective reflection coefficient would further improve the attenuation length. More importantly, the fibre-to-fibre fluctuations in the reflection coefficient and thus in their response, are very large. This is very bad, mainly for the e.m. performance (signal uniformity, energy resolution).

Much better results were obtained by giving each fibre its own individual mirror, by aluminium-plating their exit surface using a sputtering technique. This method gave excellent results for the reflectivity, for the fibre-to-fibre fluctuations in the response and for the quality of the aluminized surface (e.g. robustness).

Figure 5 shows the distribution of the reflection coefficients measured on a large sample of fibres treated in this way. The reflection coefficient was found to be $85\% \pm 4\%$. The measured effective attenuation lengths increased correspondingly.

The fibres are delivered in batches which correspond to the preform (and even the part of the preform) from which they were drawn. The optical characteristics (light yield, $\lambda_{att}$) of fibre samples ($5-10\%$) are measured, and modules are filled with fibres from batches that show similar characteristics, in order to further reduce the fibre-to-fibre fluctuations within each module.

### *3.2.2 The light collection*

The quantum efficiency of common PM photocathodes may typically vary by a factor of 2 over the sensitive area. In order to distribute the light over the photocathode area, the fibres were coupled to the PM through a plexiglass light guide. By avoiding direct optical contacts, large emittance angles from the fibre are suppressed.

In initial tests, we used circular cylindrical light guides with an aspect ratio 3:1 for this purpose. It turned out, however, that these light guides themselves introduced an important lateral non-uniformity, in the form of a signal reduction for the fibres located near the edge of the light guide. The light from fibres

located close to the edge undergoes on the average several reflections at the interface plexiglass-air (helical light path), with some loss of light. The light from the fibres facing the central part of the light guide suffers less from this phenomenon. This results in a non-uniform response.

The mentioned effect is typical for a *circular* cylindrical light guide. Other shapes (square, hexagonal) were found to improve the uniformity considerably. In fig. 6 the results are shown of scans with a fibre across the surface of light guide/PM combinations. The light guide was a cylinder with either a circular or a hexagonal cross section, the PM was always the same one. The edge effects are considerably more pronounced for the circular one.

Also the length of the light guides can be optimized (fig. 7). For short lengths, the photocathode inhomogeneities strongly determine the response; for lengths beyond the optimum value an inverted, smoothed image of the photocathode inefficiencies was observed. Figure 7 shows that in the optimal case the PM response is constant to within 1% over the full light guide surface covered by the fibres.

The PM used for all these tests was particularly non-uniform: The photocathode efficiency varied by more than a factor of 3 within the sensitive area. This amplified possible non-uniformity effects, and allowed us to cure them. The actual PM's used for our detector were selected on uniformity of the photocathode efficiency. We used custom-selected 8-stage Philips PM's (XP2282) with a gain between $10^4$ and $10^5$ in the linear regime. This relatively low gain is adapted to the large light yield of the detector ($\sim$ 1000 photo-electrons/GeV), a consequence of the fact that no external wavelength shifters are needed.

In order to check the uniformity of the response over the calorimeter surface, we measured the signal of a strongly collimated $\beta$-source ($^{90}$Sr), which was moved in small steps between the centres of two adjacent calorimeter modules. The results are shown in fig. 8, and are considered very satisfactory.

## 4. TEST BEAM RESULTS.

### *4.1 Experimental setup*

The experimental results described in this section were obtained with particle beams from the Super Proton Synchtotron at CERN. We used negatively charged electrons, pions and muons in the energy range 10 - 150 GeV for our tests.

The following detector configurations were studied:

*a*) A stack of three e.m. modules, $26.6X_0$ deep, each containing 1141 SCSN-38 fibres of 1 mm diameter. Each two modules had one common face (fig. 9). These modules were made with the casting method (sect. 3).

*b*) A similar stack, with one of the three modules having a *projective* geometry. This module was made pyramidal in one plane by machining two opposite faces under $2^0$ with the fibre axis (fig. 10). As a consequence, the fibres near these machined faces start only after a certain depth inside the calorimeter. One of the faces was machined such that the fibre density is *maximized* near the shower maximum, in the other one the fibre density is *minimized*. This module, made with the extrusion method, was studied in view of the application in a $4\pi$ geometry, which requires a pyramidal module structure.

*c*) A stack consisting of 7 small e.m. modules, $24.6X_0$ deep, each containing 397 SCSN-38 fibres of 1 mm diameter. The stack had one central module, surrounded by 6 identical ones (fig. 11). It was made with the epoxy technique (sect. 3).

*d*) One long hadronic module, containing 1141 SCSN-38 fibres of 1 mm diameter. During the tests, these fibres were replaced by slower, but more radiation-hard 3-HF ones, an operation which took less than one day. The module was made with the casting method (sect. 3). Its length amounted to 2 m ($9.5\lambda_{int}$, the length of the full hadronic calorimeter under construction) in some of the tests described, and 1.6 m ($7.5\lambda_{int}$) in other tests.

The various detector configurations were mounted on a table that could move in the plane perpendicular to the beam (x-y directions) and rotate in the horizontal plane, thus varying the angle $\theta_z$ between the fibre axis and the beam.

The measurements were performed with or without a preshower counter installed a few centimeters upstream of the detector to be tested. The preshower counter consisted of a lead absorber, $2.6X_0$ thick, followed by a scintillation counter.

The readout of the detector signals was triggered by a scintillator telescope. Proportional wire chambers installed in the beam line made it possible to locate the impact point of the beam particles with an accuracy of about a millimetre.

The beam intensity amounted to typically 100-1000 Hz, sufficiently low not to worry about a rate-dependent PM gain.

The telescope counters and the beam chambers were also used to make sure that the detector was hit by *single* particles. Apart from that, no other off-line cuts were applied in the data analysis.

*4.2. Angular scans*

A crucial feature of the spaghetti calorimeter, its hermeticity, is achieved because of the fact that the fibres are oriented longitudinally, *i.e.* they are running in the same direction as the particles that they should detect. This makes it possible to mount all the readout at the back end of the detector, thus avoiding the cracks that are inherent to sandwich structures. However, because of this feature, the showers are sampled in a way that at first sight may seem extremely non-optimal and maybe even dangerous, since large differences in signal might occur depending on the impact point of the particle (lead or fibre).

We measured the calorimeter response as a function of the angle $\theta_z$ between the incoming particle and the fibre direction, in order to investigate its influence on the energy resolution.

*4.2.1 Electrons*

In fig. 12 the signal distributions are given for 40 GeV electrons, measured in one of the $26.6X_0$ deep e.m. modules at various angles $\theta_z$. For angles of $2^0$ and above, the signal distribution is perfectly gaussian, but when the angle approaches $0^0$ deviations from a symmetric shape rapidly increase. At $\theta_z = 1.5^0$, a high-energy tail starts appearing, which becomes more pronounced at smaller angles. At angles below $0.5^0$, we also see signals with a small pulseheight.

These anomalous signals are entirely due to particles impacting on the calorimeter surface at a fibre position. This is illustrated in fig. 13. With the aid of the beam chambers a circular region of 1 mm diameter was defined within the beam spot for the measurements done at $\theta_z < 0.15^0$. This region was moved across the calorimeter surface in steps of 1 mm. The figure shows the signal distributions measured for a sequence of 3 such steps. In the left and right hand diagrams, the beam particles enter the calorimeter surface in the lead. The signal distributions are narrow and symmetric. In the middle diagram, the electrons enter the module at a fibre position. Having isolated the process that generates them, all the anomalies observed for $0^0$ in fig. 12 now appear amplified.

The anomalous signals can be explained as follows. The radiation length of polystyrene is $\sim 40$ cm and, therefore, electrons that enter the calorimeter at a fibre position under a small angle with the fibre axis can travel quite a distance before the shower starts developing. When this happens, the module is too short to fully contain the shower and some fraction of the energy will leak out at the rear end. For example, at $\theta_z = 1^0$, electrons may travel up to 5.7 cm (or $8X_0$)

in the plastic before entering the lead, which makes the effective length of the module considerably shorter.

Contrary to what one might expect, shower leakage will produce a signal that is *too large* in this type of detector, because of the following reason. Inside the detector, the sampling fraction for e.m. showers is very small, 2.3% (EGS4 simulations). However, particles leaking out at the back traverse a region with only fibres, which are bunched towards the light detection system, and are therefore sampled at essentially 100%. In other words, shower leakage is considerably amplified and leads to anomalously large signals.

At extremely small angles, this *channeling* effect may also cause anomalously *small* signals, namely if the electron traverses the whole length of the calorimeter ($26.6X_0$) without starting a shower. This effect is indeed only observed for angles of at maximum a few milliradians.

Although longitudinal shower leakage is an important effect contributing to the small-angle phenomena shown in fig. 12, it is not the only source of signal anomalies that occur when $\theta_z$ is close to zero. This is illustrated in fig. 14, which compares electron shower signal distributions at small $\theta_z$ values for a $26.6X_0$ and a $266X_0$ deep module. Longitudinal shower leakage should be completely negligible for the latter detector.

Indeed, the signals with small pulse height observed for very small angles in the short module are completely absent in the long one, confirming shower leakage as the unique origin of their occurrence. However, at the high-energy side deviations from a symmetric line shape are also observed in the long module, although the gaussian response is maintained down to smaller $\theta_z$ values than for the short module.

This asymmetric response was also confirmed by EGS4 calculations for infinitely deep modules. Such calculations also explain the at first sight amazing fact that these calorimeters work so well at angles $\theta_z$ only slightly different from zero. Fig. 15 shows the angular distribution of the particles ($e^+$ and $e^-$) through which the energy of a high-energy electron, showering in a block of dense matter, is deposited. The vast majority of these particles have an angular distribution flat in $cos\theta$, which means that they have completely "forgotten" the direction of the incoming particle. They are numerously created by Compton- or photoelectric processes in the last generations of the shower development and (the fluctuation in) their contribution to the signal of a sampling calorimeter is *independent* of the orientation of the active calorimeter material with respect to the direction of the incoming particles.

A small fraction of the particles through which the shower energy is deposited show up near $cos\theta = 1$, i.e. their direction is the one of the particle that initiated

(apex-to-apex).

In order to determine to what extent channeling effects at small angles play a role for $\mu$-detection, we determined the signal distributions for various angles $\theta_z$ and for muons impacting in different regions of the detector. The relation between the calculated path length in the module and the measured signal (the most probable value obtained from the Landau fit) is given in fig. 17. There is a strong correlation between both quantities, which has to be expected if the differences observed in the signal distributions have a purely geometric origin. The fact that the width of the Landau distribution at $0^0$ is significantly larger than at $1^0$ (at which angle the muons are also almost fully contained in the module) might be an indication that some channeling *does* occur at very small angles (see fig. 16). More detailed studies are needed for this.

Figure 16 also shows that the signal/noise ratio of this detector is such that an accurate measurement of the energy loss by muons is possible. For this, one needs however first to determine the $e/mip$ signal ratio, which requires a careful analysis of muon signal distributions at different energies[1] . This will be the subject of a future study.

### *4.3. Energy resolution for e.m. showers*

Signal distributions for 40 GeV electrons incident on a $26.6X_0$ deep module were already given in fig. 12, as a function of $\theta_z$. For $\theta_z \geq 2^0$, excellent fits to a gaussian distribution were obtained. As a standard procedure, we fitted the signal distributions over the range $<$ mean value $\pm 2\sigma >$.

The energy resolution $\sigma/E$ obtained in this way for 40 GeV electrons is given in fig. 18, as a function of $\theta_z$. The resolution varies only a little with $\theta_z$ down to $\sim 4^0$. For smaller angles, the energy resolution deteriorates quite rapidly.

Measurements of electron signal distributions were also done at 10, 20, 80 and 150 GeV. In fig. 19 the energy resolution $\sigma/E$ is given as a function of the electron energy, at three different $\theta_z$ values ($3^0$, $5^0$ and $8^0$). The energy is given on a scale linear in $E^{-1/2}$. If the energy resolution were only dependent on purely statistical factors, i.e. if systematic effects would not contribute, the measured points should follow a straight line which extrapolates to a resolution of 0% at infinite energy in this graph. Several examples of such lines, corresponding to energy resolutions of $10\%/\sqrt{E}$, $15\%/\sqrt{E}$, etc. are included in the figure. It turns out that systematic effects are not completely absent. They manifest themselves as a constant term contributing to the energy resolution. The value of this term

can be estimated by extrapolating the fitted curves through the experimental points to infinite energy.

The experimentally measured energy resolutions were fitted to curves of the type $\sigma/E = a + b/\sqrt{E}$. Such fits gave excellent $\chi^2$ values. The results are shown in fig. 20, where the values of $a$ (the constant term) and $b$ (the statistical term) are given as a function of $\theta_z$. It turns out that the term scaling with $E^{-1/2}$ is only very slightly dependent on $\theta_z$, with values for $b$ of $13 - 14\%$.

On the other hand, the contribution of systematic effects to the energy resolution (the value of $a$) was found to be rather sensitively dependent on $\theta_z$. For $\theta_z \geq 5^0$, the contribution of such effects was found to be 1% or less, but for smaller angles $a$ rises, reaching $\sim 1.5\%$ at $2^0$.

At energies above $\sim$ 100 GeV, the energy resolution for e.m. showers is, therefore, dominated by systematic effects. We have identified at least one source of such effects: the casting method (sect. 3.1). Lead has a considerable thermal expansion coefficient, so the forces that are active during the solidification and cooldown over a temperature trajectory of more than $400^0$C may lead to non-negligible displacements of the stainless steel housing of the fibres.

This is illustrated in fig. 21a, where a lateral cross section of a module made in this way is shown. It is clear that the effects mentioned above have caused the tubes (and thus the fibres) to be distributed according to a very irregular pattern. As a consequence, the number of fibres in a given volume will depend on the position of this volume inside the detector. Therefore, the *sampling fraction* and thus the signal of e.m. showers detected in this module will depend on the volume in which the shower develops.

We also did measurements on a module made with the extrusion method. A cross section of such a module is shown in fig. 21b. Here, the fibre pattern is very regular. The value of $a$ obtained from a fit to the $3^0$ data obtained with this detector was significantly lower than with the cast module (fig. 20).

Also among the various cast modules we found differences in the values of $a$. In the case of the module for which the experimental results are shown in figs. 18-20, the stainless steel tubes were kept together by 3 spacers, one in the center of the module and one at each end. Therefore, the distance between places where the tubes were held in a fixed position amounted to 10 cm. For other modules, the central spacer was omitted and, therefore, the amplitude of potential displacements was quadrupled. The constant term $a$ in the e.m. energy resolution was found to be considerably larger for these modules.

The fluctuations in the sampling fraction will not only affect the achievable energy resolution, but also the signal uniformity across a module (see sect. 4.4).

Since they dominate the calorimeter performance at high energy, they should be avoided and, therefore, we have decided to build our final detector with modules made with the extrusion method.

There are several other factors that contribute to the constant term $a$, which limits the e.m. calorimeter resolution at high energies. Among these, we mention noise in and stability of the PM and readout electronics, stability of the high-voltage supply, etc. Another important factor is the variation in the response from fibre to fibre. It was shown in a previous paper[15] that, in order to limit the contribution from this source of fluctuations to the e.m. energy resolution to 1%, the fibre-to-fibre response should not vary by more than $\sim$ 6%. This rather severe requirement is a consequence of the relatively small number of different fibres contributing to the signal for a given shower. When the angle $\theta_z$ is increased, more fibres participate in the signal, and the contribution of fibre-to-fibre response fluctuations to $a$ decreases. This is in agreement with the experimental observations (fig. 20) which show a decreasing value of $a$ for increasing $\theta_z$.

### *4.4 Signal uniformity*

Signal uniformity and energy resolution go hand in hand. High local energy resolution does not help if the signal variations with the impact coordinates are much larger.

Several factors that limit the e.m. energy resolution, in particular the high-energy performance (i.e. the constant term), also affect the signal uniformity. Among these we mention the fluctuations in the sampling fraction and in the fibre-to-fibre response. Such effects may be particularly harmful if they are not random. An example is the non-uniformity in the light collection, which we solved by properly choosing the shape and dimensions of the light guide (sect. 3.2.2). Also, the variations in sampling fraction occurring in the cast modules turned out to have non-random aspects, for example the fact that the fibres tend to cluster in groups of 3 in certain regions (fig. 21a).

In fig. 22a, results are shown of a scan with 40 GeV electrons between the centres of two adjacent modules, called C and A. The figure shows the average signal in both modules and their sum as a function of the beam position. Both modules were made with the casting method, the difference being that module C had a central spacer, which limited the amplitude of tube diplacements during the production process (see sect. 4.3). The figure shows that the signal uniformity in this module is considerably better than in the other one, as is the energy

resolution (fig. 22b).

These results are not in contradiction with the ones shown in fig. 8, which were obtained for a similar scan with a $\beta$-source. The electrons from this source only penetrated a few millimetres into the module, in the immediate vicinity of the spacer, i.e. in the region where the sampling fraction was guaranteed to be constant in any case.

Considerably better results were obtained with modules that were made with the extrusion method. In fig. 23 the signal and the energy resolution are shown for a scan with a 40 GeV electron beam moving in small steps between the centres of two adjacent modules, one of which had a projective structure (stack *b*, see sect. 4.1). The signal is very uniform and, even in the region where the beam hits the boundary between the 2 modules, it is hardly affected (variation less than 3%). We did not see any significant difference between the results for the 2 different surfaces of the projective modules (see sect. 4.1). Also the energy resolution is very constant over the full scanned region, so that one may conclude that the electrons virtually don't notice that they are being detected with a modular device.

### *4.5 Signal linearity*

The linearity of the response to e.m. showers was measured for both long (1.6 m, $7.5\lambda_{int}$) and short (20 cm, $26.6X_0$) modules, using electrons with energies from 10 - 150 GeV. The results were compatible, indicating that the effect of longitudinal shower leakage in the short modules on the signal linearity is negligibly small.

The results are shown in fig. 24, where the signal per unit energy is given as a function of the energy for e.m. showers measured in a 1.6 m long calorimeter module. Since we are looking for small effects, we tried to determine the energy of the beam particles as accurately as possible, rather than using the nominal values. As a basis, we used the actual current in the last (momentum-defining) bending magnets of the beam line. (Small) corrections for the loss due to synchrotron radiation were made. The data points were obtained as the ratio of the average ADC values of the electron signals and the calculated beam energy. Deviations from linearity were found to be smaller than 1%.

The beam energy also depends, apart from on the magnet current, on hysteresis effects and, therefore, on the history of the magnet settings. For accurate measurements, one should in fact demagnetise all the magnets before changing the energy. Since this was not done, the beam energy suffers from an intrinsic

uncertainty, which is of course relatively largest at low energies (low magnet current). This uncertainty is represented by the 2 dashed lines in fig. 24, which include apart from the hysteresis effects (184 MeV) also a 0.2% uncertainty in the linearity of the current/energy relationship.

We conclude from these measurements that the calorimeter is linear for detecting e.m. showers, at the level of the accuracy with which the electron beam energy is known.

### *4.6 Electron/pion separation*

One of the most important tasks of modern calorimeters is the identification of leptons, both at the trigger level and off-line. The classical method to identify electrons with calorimetric information is based on exploiting differences in the energy deposition profiles of e.m. and hadronic showers. Both the longitudinal and lateral shower profiles can be used for this purpose.

The structure of our detector makes a subdivision into various longitudinal segments a rather unelegant, although not impossible, option.

In a previous paper[12] we demonstrated that, thanks to the extraordinary signal speed of our detector, a completely new method for $e$-identification could be used. This method is based on exploiting subtle differences in the *time structure* of e.m. and hadronic shower signals, which occur on a 5-10 ns time scale and allow $e/\pi$ separation at the 1% level.

In fact, the time structure of the signals contains longitudinal shower information. This is illustrated in fig. 25, where some typical 80 GeV pion signals are shown. The signal displayed in fig. 25a reveals a double-hump structure, characteristic for a hadronic shower that starts developing at some depth inside the calorimeter. The signal of the light trapped in the direction of the PM (the first peak) and of the light going in the opposite direction and being reflected at the aluminized open end of the fibres (second peak) are separately visible. For showers that start developing more upstream in the module, the second hump follows more and more closely the first maximum (fig. 25b). This results in a decrease of the corresponding signal width (expressed e.g. in terms of the full width at a certain fraction of the amplitude). Some signals show, within the resolution of our digitizing oscilloscope (1 ns), no distinguishable second hump at all (fig. 25c), indicating pions that start showering very early in the module. The latter signals are harder to distinguish from electron shower pulses, especially also because at 80 GeV a large fraction of the energy goes into $\pi^0$ production, mostly close to the shower axis, i.e. inside the module whose signal is displayed

here. When moving away from the axis, the energy will be deposited, on average, more deeply inside the detector. Moreover, the relative contribution of neutrons, which are also expected to stretch the signal, will increase. Therefore, we expect to be able to further improve the $e/\pi$ separation through the time structure of the signals if signals from a larger radial area around the shower axis are analysed.

This type of data has great potential for very fast triggering on e.m. showers, which is, in our opinion, more important than the longitudinal shower information it provides. The information can in principle be acquired on a time scale compatible with the signal duration itself, i.e. $\sim$ 20 ns, thus avoiding the time-consuming processing of energy deposit patterns needed when the electron identification is based on shower profile data. We are developing special electronics for this purpose.

Disregarding the signal shape, measurements were also performed to study the identification power for isolated electrons with a 1.6 m long unsegmented module, preceded by a $2.6X_0$ lead converter read out with a scintillation counter.

In fig. 26, the signal distributions for 40 GeV electrons and pions measured in this preshower counter are given, illustrating the discriminative power of this device.

In fig. 27, the signal distributions for high-energy (150 GeV) electrons and pions in the fibre calorimeter are given. It is interesting to note that even this pencil-type detector works already as a reasonable calorimeter for high-energy hadron detection. If we assume that the detector is compensating, $\sim$ 50% of the pion energy is deposited in this module (a 48cm$^2$ cell). The width of the distribution ($\sigma/E \approx 20\%$) is probably reflecting the spread in the fraction of the energy carried by $\pi^0$'s. The remaining $\sim$ 50% of the pion energy is deposited in neighbouring cells.

A very small fraction of the pions give a signal equal to that of an electron at the same energy, which is laterally contained in the module. This fraction of the pion events can, therefore, be confused with electrons.

We used these sources of information, i.e. the preshower signal and the lateral shower containment, to determine the $e/\pi$ separation capability of our detector setup. In total, $\sim 2.10^5\pi^-$ and $\sim 10^4 e^-$ at 80 GeV were used for this purpose. We determined which fraction of the pions gave rise to a signal in both the preshower counter and the calorimeter that could be confused with that of an electron. The results depend of course on the cuts applied. These cuts may also have the consequence that a certain number of genuine electrons do not pass the selection.

In fig. 28, the fraction of pions that pass the selection criteria for an electron

is plotted versus the fraction of electrons passing the same cuts. It turns out that while, for example, only $5.10^{-4}$ of the pions are identified as electrons, 98% of the genuine electrons are retained. We found that the inclusion of time structure data only marginally improved the $e/\pi$ separation capability. This may either mean that this data is strongly correlated to the shower profile information, or that the pion beam contained some electron contamination.

In order to investigate the latter possibility, we also took data with the pion beam passing through 5 cm of lead, placed $\sim$ 300 m upstream from the detector. From a comparison of the signals, we determined an upper limit on the electron contamination of the pion beam, which was compatible with the $e/\pi$ separation capability obtained from the previous analysis. Therefore, the results shown in fig. 28 should be interpreted as an upper limit: the actual $e/\pi$ separation achievable for isolated particles with our longitudinally unsegmented calorimeter plus the preshower counter system is equal or better than indicated in this figure.

On the other hand, it should be emphasized that the chosen experimental setup, with the particles entering the module at its axis so that e.m. showers are (almost) fully contained, represents a favourable situation. In general, also the e.m. shower energy will be shared by several modules. Moreover, the present study was done with only one module, which requires using the known beam energy and assuming compensation in order to obtain results. More detailed studies with a multi-module detector, where criteria based upon energy sharing between neighbouring modules can be used, are needed for determining the full $e/\pi$ separation capability of this technique.

## 5. CONCLUSIONS.

We have tested in detail the performance of prototype modules for a new type of calorimeter, intended to be used as an integrated $4\pi$ e.m./hadronic calorimeter in a high-luminosity environment. The detector consists of lead as absorber material and scintillating plastic fibres with 1 mm diameter as active material. Passive and active material are mixed in a volume ratio 4:1, such as to achieve compensation.

Our goal is to be able to measure jets, electrons and missing energy with an accuracy of $\sim$ 1%. Strangely enough, it may turn out that this goal is hardest to achieve for electrons, the subject of the investigations described in this paper. Because of the small sampling fraction (required because of compensation) and the very short radiation length of the detector (7.5 mm), the area in which the shower develops, and thus the number of different fibres contributing to the signal,

is small. And, therefore, the performance is very sensitive to factors like fibre-to-fibre response fluctuations, uniformity of the light collection and variations in the sampling fraction. We have encountered all these problems, and have found adequate solutions.

The results achieved to date, with some room left for further improvement, are as follows:

*i*) Energy resolution for e.m. showers $13\%/\sqrt{E}$, with a constant term of $\sim 1\%$ for $\theta_z = 3^0$.

*ii*) Signal non-uniformity and boundary effects smaller than 3% for projective modules that are realistic for application in a $4\pi$ geometry.

*iii*) Signal linearity for e.m. shower detection better than 1%.

*iv*) Electron/pion separation for unsegmented detector modules (but with the use of a preshower counter) better than $5.10^{-4}$, with 98% of the electrons passing the cuts, for isolated particles.

The problems that we had to solve in order to obtain these performance figures are expected to be much less important for hadron detection, simply because the area over which the shower develops, and the number of different fibres contributing to the signal, are so much larger. With the aid of optical filters and mirrors (see sect. 3.2.1) we obtained light attenuation lengths of 8-10 m, which *is* important for hadron showers.

The signal amplification phenomena resulting from longitudinal shower leakage, observed for e.m. showers (sect. 4.2, 4.3), are expected to be unimportant for hadron showers. The reason is that particles that leak out after 10 interaction lengths are almost exclusively neutrons. These are very efficiently (50%) sampled *inside* the detector volume, unlike charged particles.

This type of detector has some very powerful features: Hermeticity and signal speed. Hermeticity can be achieved because the fibres are oriented in the direction of the incoming particles. We found that channeling effects, which disturb the performance, can be avoided if the detector is designed such that the particles enter it at an angle of at least $2^0$ with the fibre axis. This can be achieved in practice, with negligible effects on the accuracy with which the shower position can be determined[19] .

The response of this detector is extremely fast. Figure 25 shows that we are close to the ultimate limits set by the speed of light. Apart from the fact that signal speed is crucial to handling the event rates envisaged in future hadron colliders ($\geq$ 100 MHz), this feature also offers a possibility of very fast triggering on e.m. showers, which may lead to an important reduction of the data.

And finally, the fact that our design allows very fast and easy replacement of the active material (as proven in practice) is important in view of possible radiation damage problems. This feature, together with the progress in the development of radiation-hard plastics[20] , where stability at 10 MRad is now considered feasible, makes us confident that radiation damage is a manageable problem for this detector operating at a supercollider.

Summarizing, we believe that the detector that we are developing should be considered a serious candidate for any experiment at such a machine.

## Acknowledgements

We are very much indebted to the LAA project leader, Prof. A. Zichichi, for his warm interest and encouraging support for this project. The work described in this paper would have been impossible without the outstanding technical support provided by our technicians O. Barnaba, S. Bricola, J.-M. Chapuis, A. Freddi, G. Iuvino, G. Pontoriere, L. Rose-Dulcina, G. Sannier, A. Sigrist and V. Vanzanella. Financial support from the Istituto Nazionale di Fisica Nucleare to the Cagliari, Napoli and Pavia groups is acknowledged. And finally, we are grateful to the staff of the SPS for the excellent beam conditions provided during our tests.

# REFERENCES


1. T. Akesson *et al.*, Nucl. Instr. and Meth. **A262** (1987) 243.
2. S. Aronson *et al.*, Nucl. Instr. and Meth. **A269** (1988) 492.
3. The ZEUS Detector, Technical Proposal, DESY, March 1986.
4. Y. Galaktionov *et al.*, Nucl. Instr. and Meth. **A251** (1986) 258.
5. UA1 Collaboration, Design Report of a U-TMP Calorimeter for the UA1 Experiment with ACOL, CERN UA1-TN/86-112 (1986).
6. C.W. Fabjan and R. Wigmans, Rep. Progr. Phys. **52** (1989) 1519, and references therein.
7. R. Wigmans, Nucl. Instr. and Meth. **A259** (1987) 389.
8. E. Bernardi *et al.*, Nucl. Instr. and Meth. **A262** (1987) 229.
9. G. d'Agostini *et al.*, Nucl. Instr. and Meth. **A274** (1989) 134.
10. H. Tiecke, Nucl. Instr. and Meth. **A277** (1989) 42.
11. H. Brückmann *et al.*, Nucl. Instr. and Meth. **A263** (1988) 136.
12. R. DeSalvo *et al.*, Nucl. Instr. and Meth. **A279** (1989) 467.
13. SSC Central Design Group, Radiation levels in the SSC interaction regions, Task Force report SSC-SR-1033, D. Groom, editor (1988).
14. C. Leroy *et al.*, Nucl. Instr. and Meth. **A252** (1986) 4.
15. F.G. Hartjes and R. Wigmans, Nucl. Instr. and Meth. **A277** (1989) 379.
16. P. Jenni, Nucl. Phys. **B3** (Proc. Suppl.) (1988) 341.
17. P. Sonderegger, Nucl. Instr. and Meth. **A257** (1987) 523, and references therein.
18. R. Kopp *et al.*, Z. Phys. **C28** (1985) 171.
19. R. Desalvo, Dream of a Supercollider Detector, Contribution to the Workshop on Calorimetry for the SSC, Tuscaloosa, March 1989.
20. S. Majewski, Talk given at the ECFA Workshop on Detectors for Supercolliders, Barcelona, September 1989.

# FIGURE CAPTIONS

1. An evaluation of the energy resolution for e.m. and hadronic showers in compensating lead/scintillator calorimeters. The energy resolution is given as a function of the sampling *frequency*, for a fixed (compensating) sampling *fraction*. The experimental points were taken from ref. 10 and from this paper.
2. The structure of a spaghetti calorimeter module ($a$), and of a large detector built with such modules ($b$).
3. The mechanical structure of a SPACAL module and its readout.
4. The calorimeter response to $\gamma$'s from a $^{60}$Co ring source surrounding the 2 m long module, as a function of the distance to the PM. The measurements were done without a filter/mirror (curve $a$), with a yellow filter ($b$), and with a filter and a (static) mirror ($c$).
5. Distribution of the reflection coefficients, measured on aluminium-plated fibres.
6. Response to a fibre scanning the surface of a light guide/PM combination. Results for circular and hexagonal cylindrical light guides with the same length, using the same PM. Note the blown-up vertical scale.
7. Response to a fibre scanning the surface of a hexagonal light guide/PM combination, for various lengths of the light guide.
8. Calorimeter response to a collimated $\beta$-source scanning the boundary between two SPACAL modules.
9. Detector configuration with 3 e.m. modules ($26.6X_0$ deep).
10. Longitudinal cross section of the pyramidal module.
11. Detector configuration with 7 e.m. modules ($24.6X_0$ deep).
12. Signal distribution for 40 GeV electrons in a $26.6X_0$ deep module, for different angles $\theta_z$.
13. Signal distributions for 40 GeV electrons hitting a $26.6X_0$ deep module oriented at an angle $\theta_z < 0.15^0$ with the fibre axis. A circular beam spot with a 1 mm diameter is moved in steps of 1 mm across the calorimeter surface. In the left and right diagrams, the particles impact on the lead in between the fibres; in the central diagram, they enter into a fibre.
14. Signal distribution for 40 GeV electrons entering a fibre calorimeter under small angles $\theta_z$ with the fibre axis. Data for a $26.6X_0$ deep module (left) and a $266X_0$ deep module (right).

15. Angular distribution of the particles (electrons and positrons) through which the energy of a showering high-energy electron is absorbed.

16. Signal distribution for 150 GeV muons in a 2 m long module, for different angles $\theta_z$.

17. The path length of muons in a 2 m long fibre detector module *vs* the resulting signal, for various values of the angle $\theta_z$.

18. The energy resolution for 40 GeV electrons, incident on a $26.6X_0$ fibre detector module, as a function of the angle of incidence $\theta_z$.

19. The energy resolution for electrons incident on a $26.6X_0$ deep fibre detector module, as a function of the electron energy. The abcissa is linear in $E^{-1/2}$.

20. The energy resolution for electrons. Shown are the results of fits of the type $\sigma/E = a + b/\sqrt{E}$, for measurements over the energy range 10 - 150 GeV, for various values of the angle of incidence $\theta_z$. The left ordinate gives the values of $a$ (circular points), the right ordinate the values of $b$ (square points). The results were obtained from measurements on modules produced with the casting method (closed points) or with the extrusion method (open points).

21. Lateral cross section, at a certain depth, of fibre modules made with the casting method (a) and with the extrusion method (b). The length of the arrow is a measure for the transverse e.m. shower size (Molière radius).

22. Results of a scan with 40 GeV electrons between the centres of 2 adjacent modules named A and C. The beam is moved in steps of 5 mm. In *a*) is plotted the average signal in both modules, and their sum, as a function of the beam position. Module A was made with the casting method, with 20 cm distance between the spacers holding the stainless steel tubes. In *b*) the energy resolution with which the electrons are detected is given.

23. Results of a scan with 40 GeV electrons between the centres of 2 adjacent modules with small or no sampling fraction fluctuations. One of the modules is cylindrical, the other pyramidal, with a projective geometry. In *a*) is plotted the average signal in both modules and their sum, as a function of the beam position. In *b*), the energy resolution with which the electrons are detected is given.

24. The signal per unit energy as a function of energy, for e.m. showers measured in a 1.6 m long fibre calorimeter module. The dashed curves reflect the uncertainty in the beam energy.

25. Typical shower signals from 80 GeV $\pi^-$, measured with a 1.6 m long fibre module (1 ns/bin

26. The signal distribution in the preshower counter for 40 GeV electrons ($a$) and 40 GeV pions ($b$).

27. Signal distribution for 150 GeV $e^-$ ($a$) and 150 GeV $\pi^-$ ($b$) in a 2 m ($9.5\lambda_{int}$) deep module.

28. The $e/\pi$ separation capability of the calorimeter/preshower counter system. The fraction of pions that pass the selection criteria for an electron is plotted versus the fraction of electrons passing the same cuts. The abcissa gives the cut-off value in the signal from the preradiator counter. Data taken at 80 GeV.

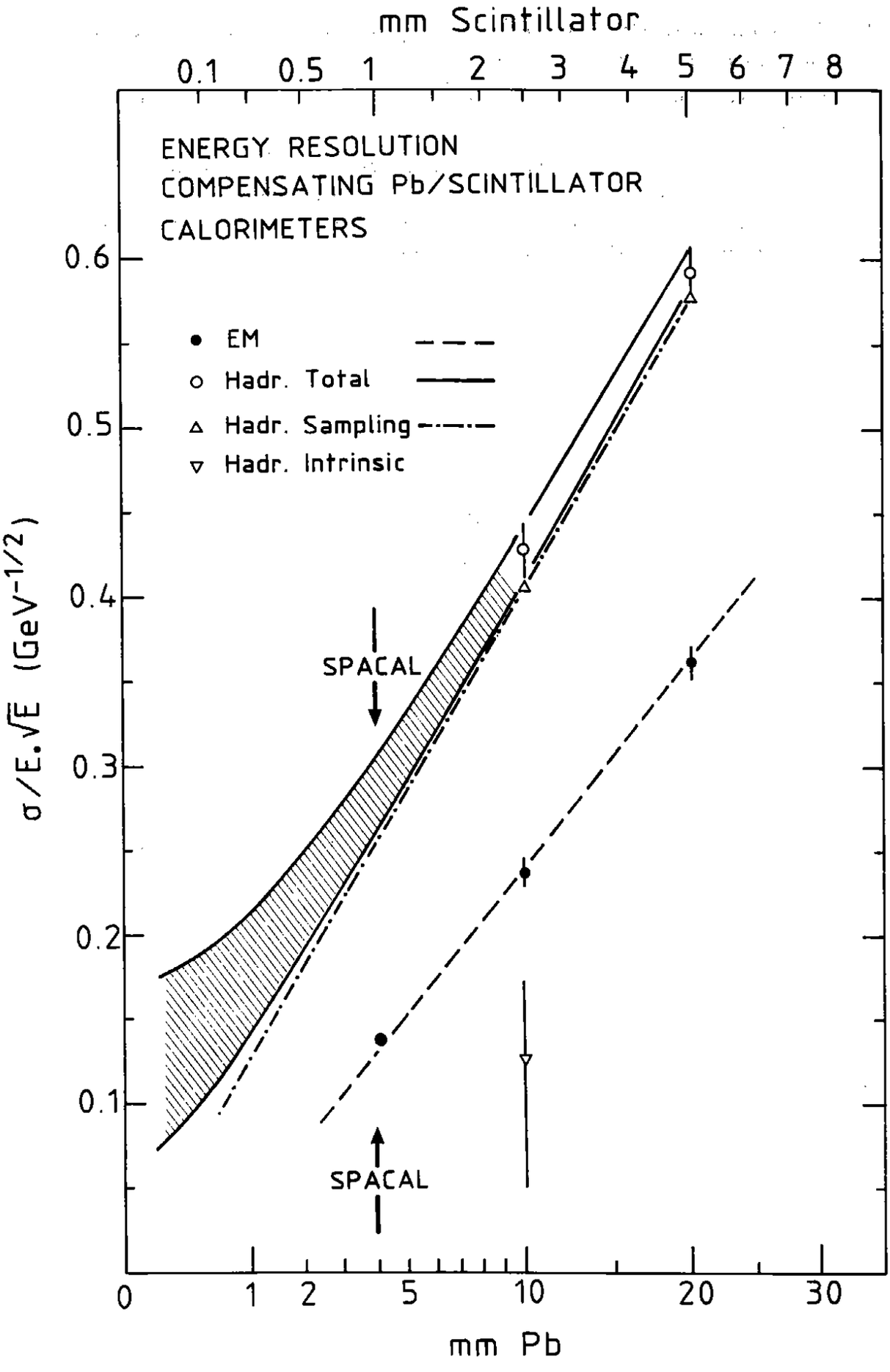
mm Scintillator
0.1
0.5
1
2
3
4
5
6
7
8
ENERGY RESOLUTION
COMPENSATING Pb/SCINTILLATOR
CALORIMETERS
EM
Hadr. Total
Hadr. Sampling
Hadr. Intrinsic
σ/E.√E (GeV^-1/2)
0.6
0.5
0.4
0.3
0.2
0.1
SPACAL
SPACAL
0
1
2
5
10
20
30
mm Pb

**Figure 1**

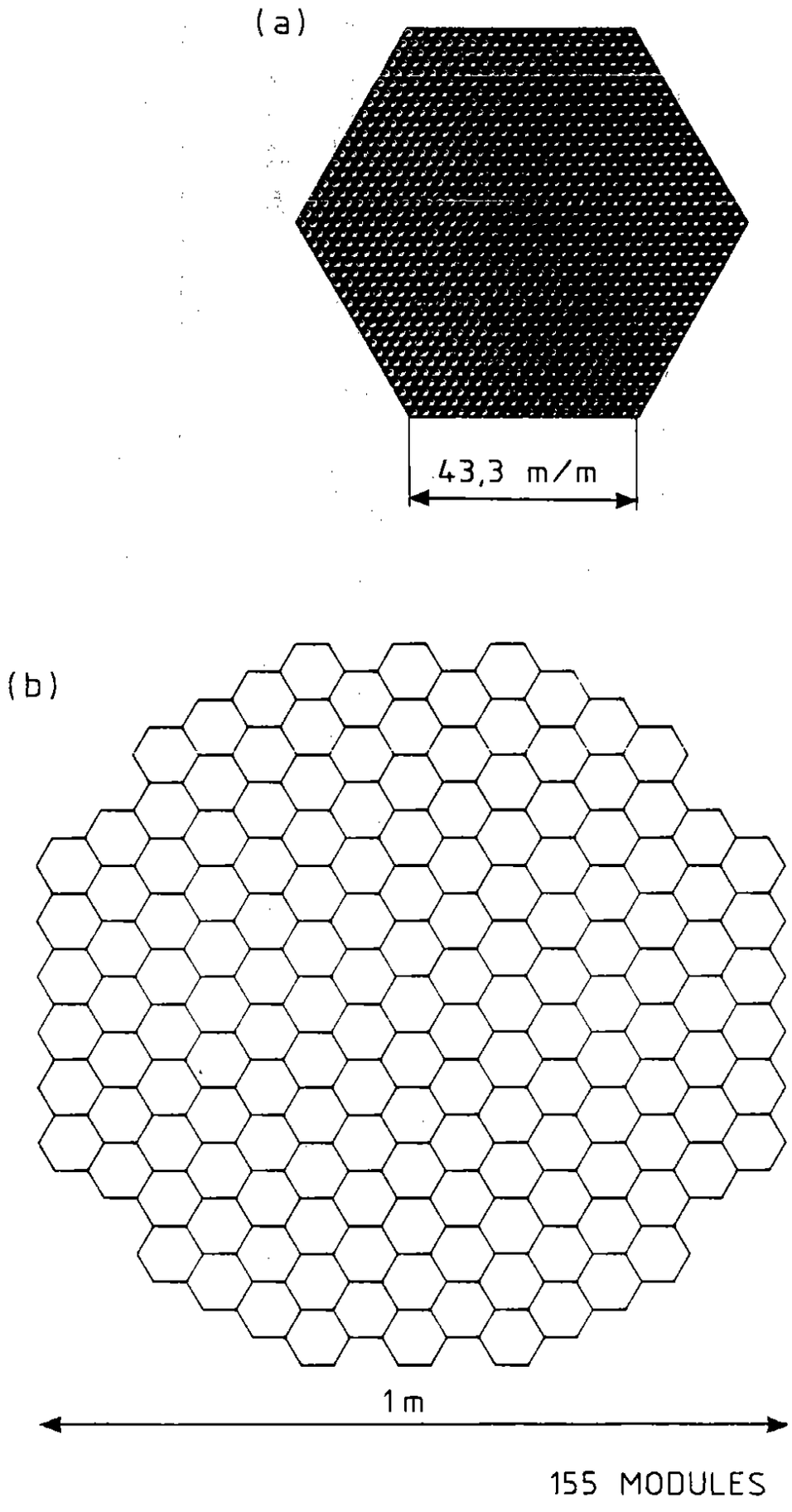


**Figure 2**

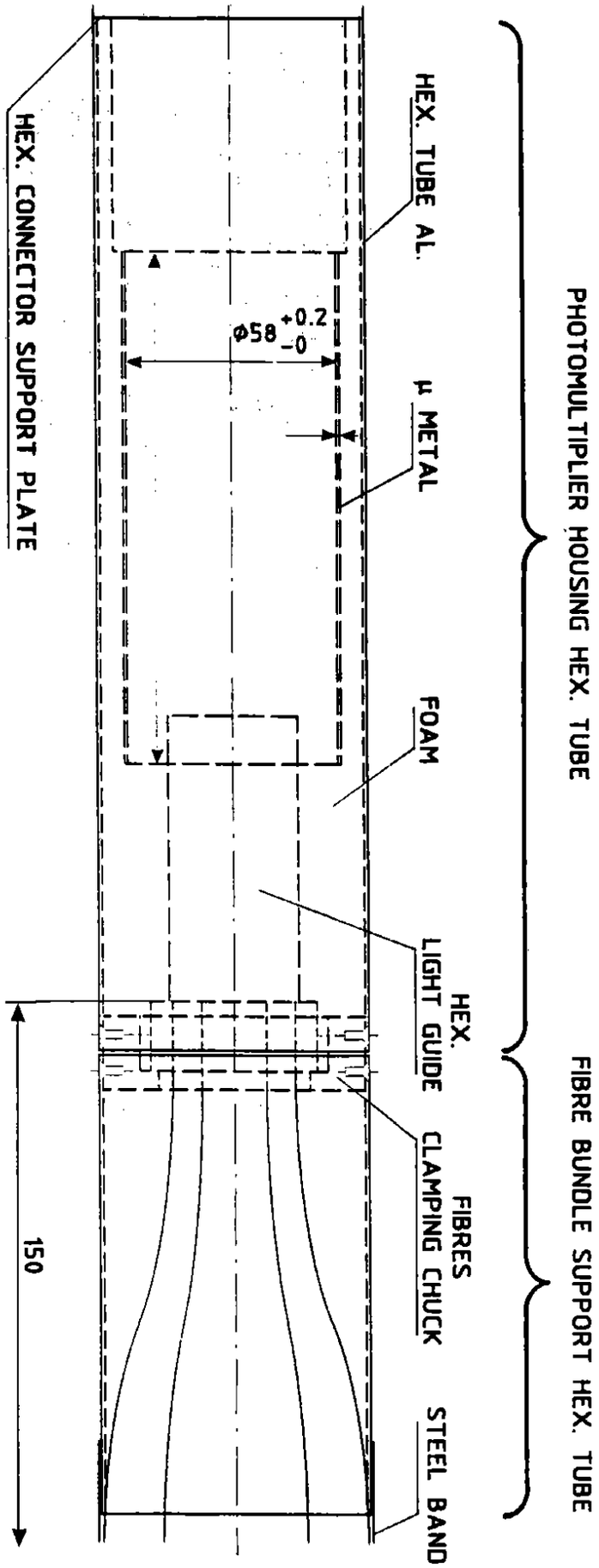
HEX. CONNECTOR SUPPORT PLATE
HEX. TUBE AL.
μ METAL
FOAM
HEX. LIGHT GUIDE
FIBRES CLAMPING CHUCK
STEEL BAND
150
PHOTOMULTIPLIER HOUSING HEX. TUBE
FIBRE BUNDLE SUPPORT HEX. TUBE

Figure 3

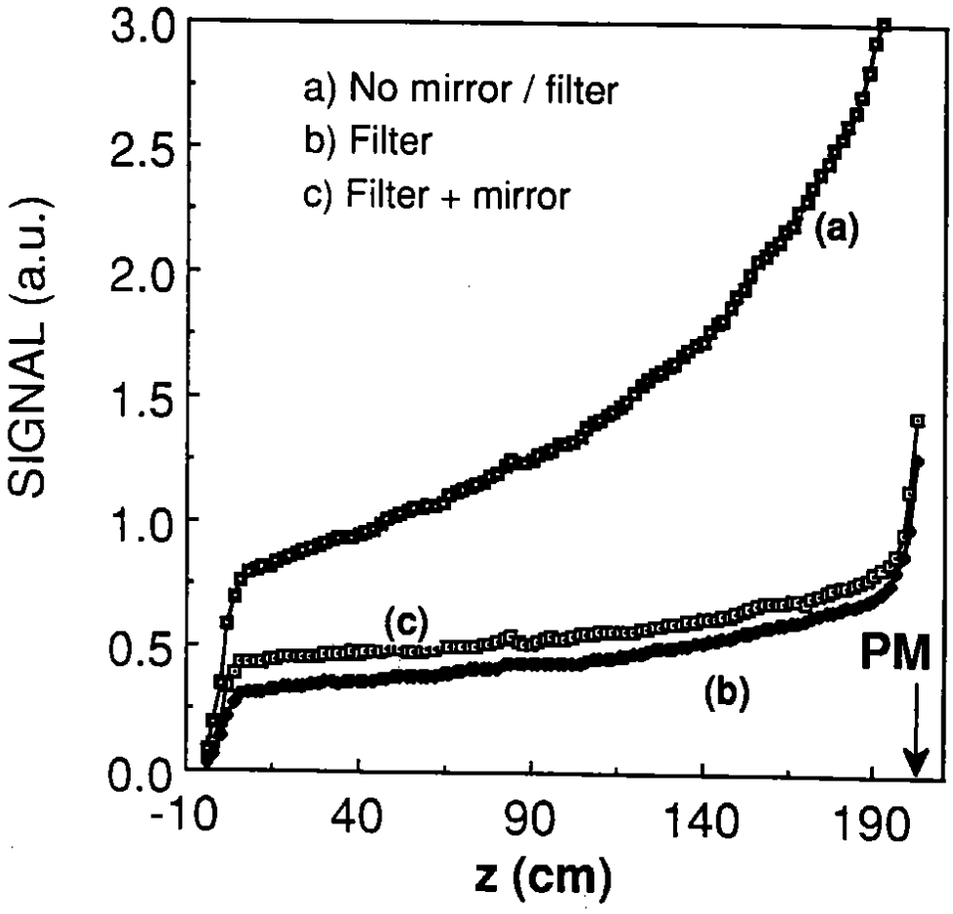
a) No mirror / filter
b) Filter
c) Filter + mirror
(a)
(b)
(c)
PM
SIGNAL (a.u.)
z (cm)
3.0
2.5
2.0
1.5
1.0
0.5
0.0
-10
40
90
140
190

Figure 4

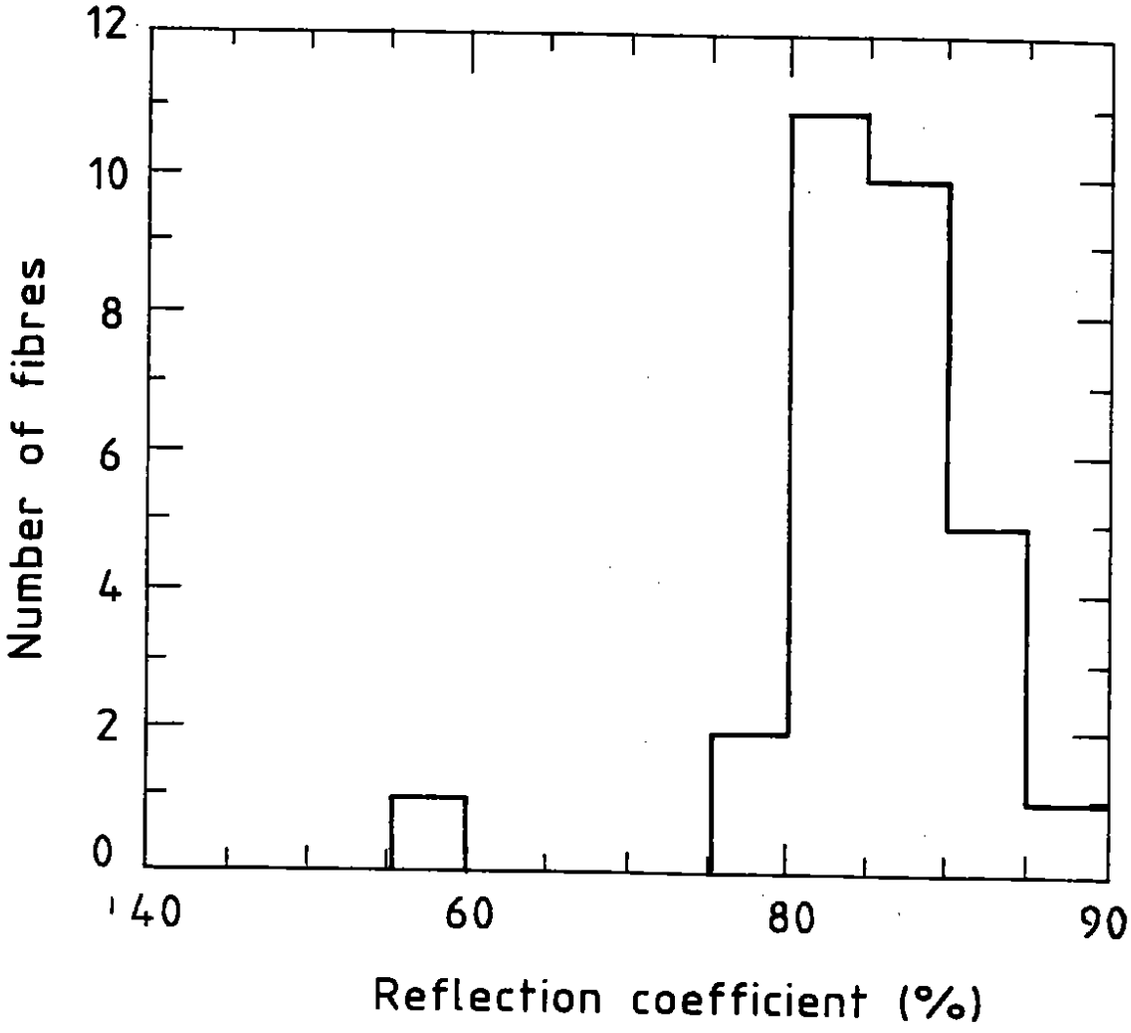
12
10
8
6
4
2
0
Number of fibres
40
60
80
90
Reflection coefficient (%)

Figure 5

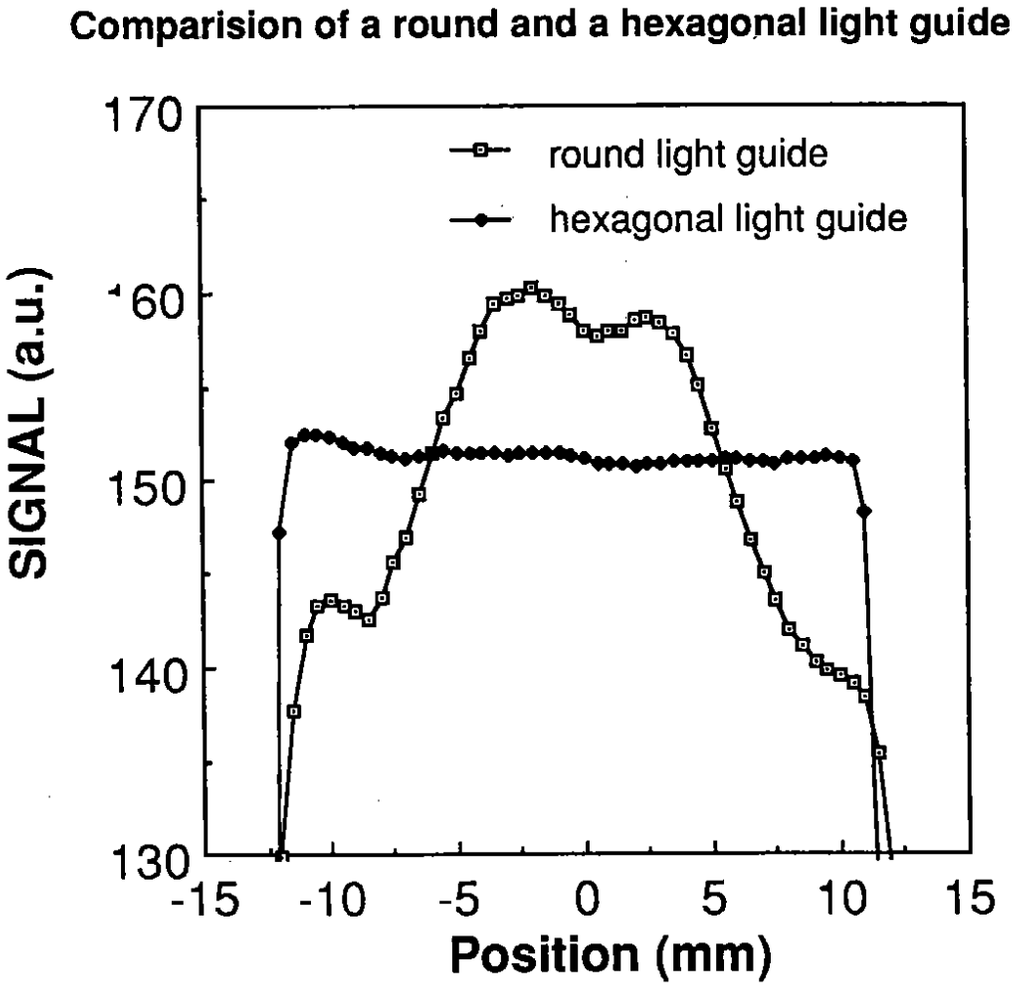
Comparision of a round and a hexagonal light guide
round light guide
hexagonal light guide
SIGNAL (a.u.)
170
160
150
140
130
-15
-10
-5
0
5
10
15
Position (mm)

Figure 6

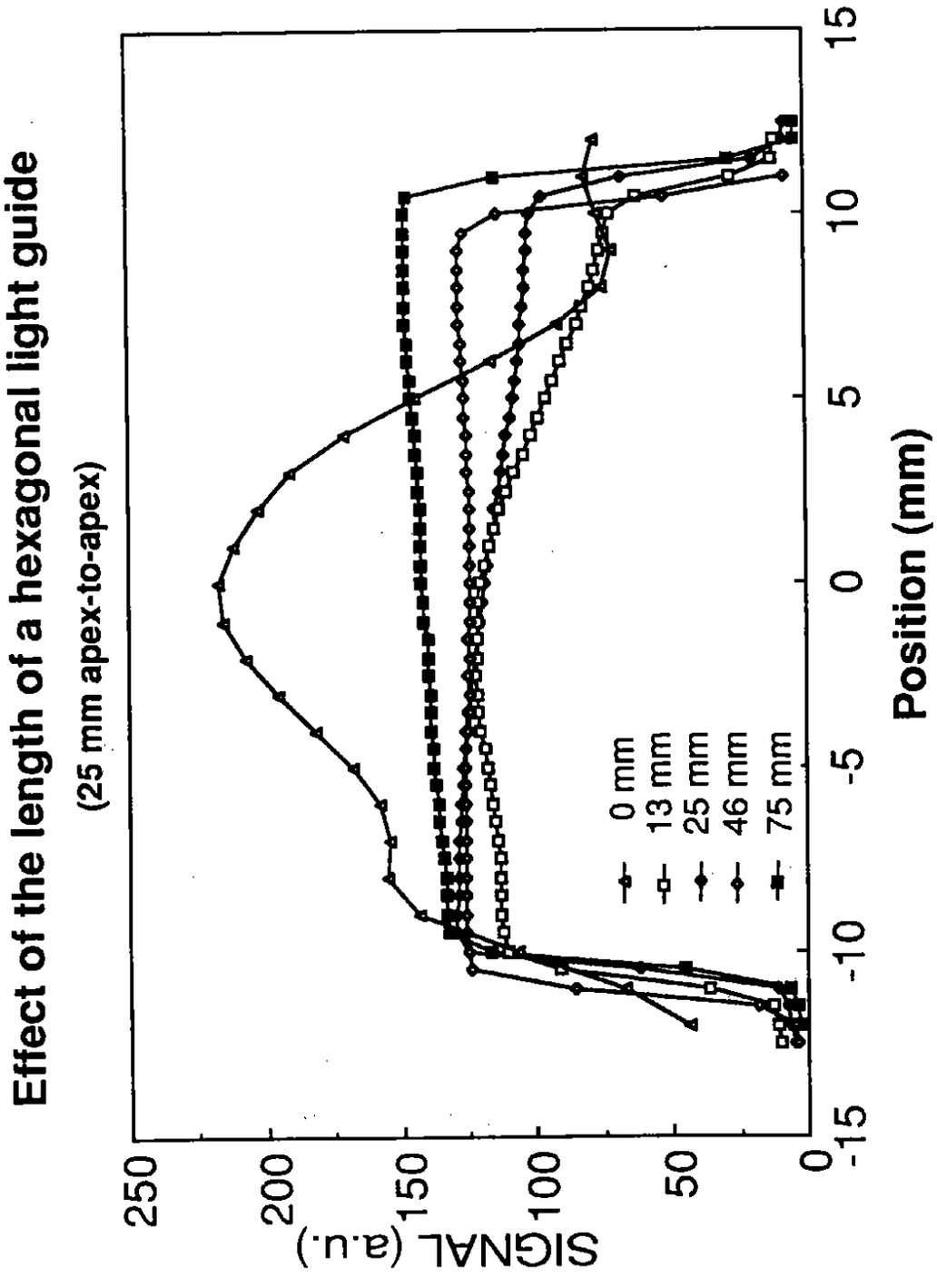
Effect of the length of a hexagonal light guide
(25 mm apex-to-apex)
SIGNAL (a.u.)
Position (mm)
0
50
100
150
200
250
-15
-10
-5
0
5
10
15
0 mm
13 mm
25 mm
46 mm
75 mm

Figure 7

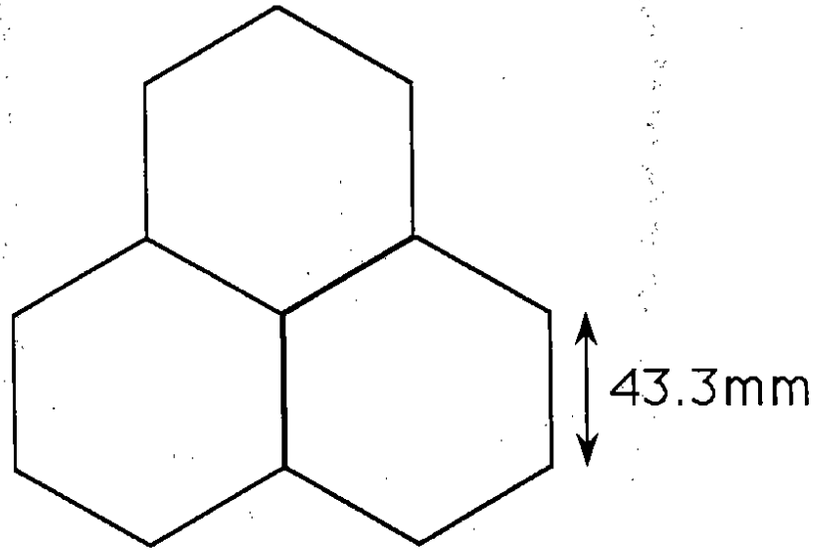


**Figure 9**

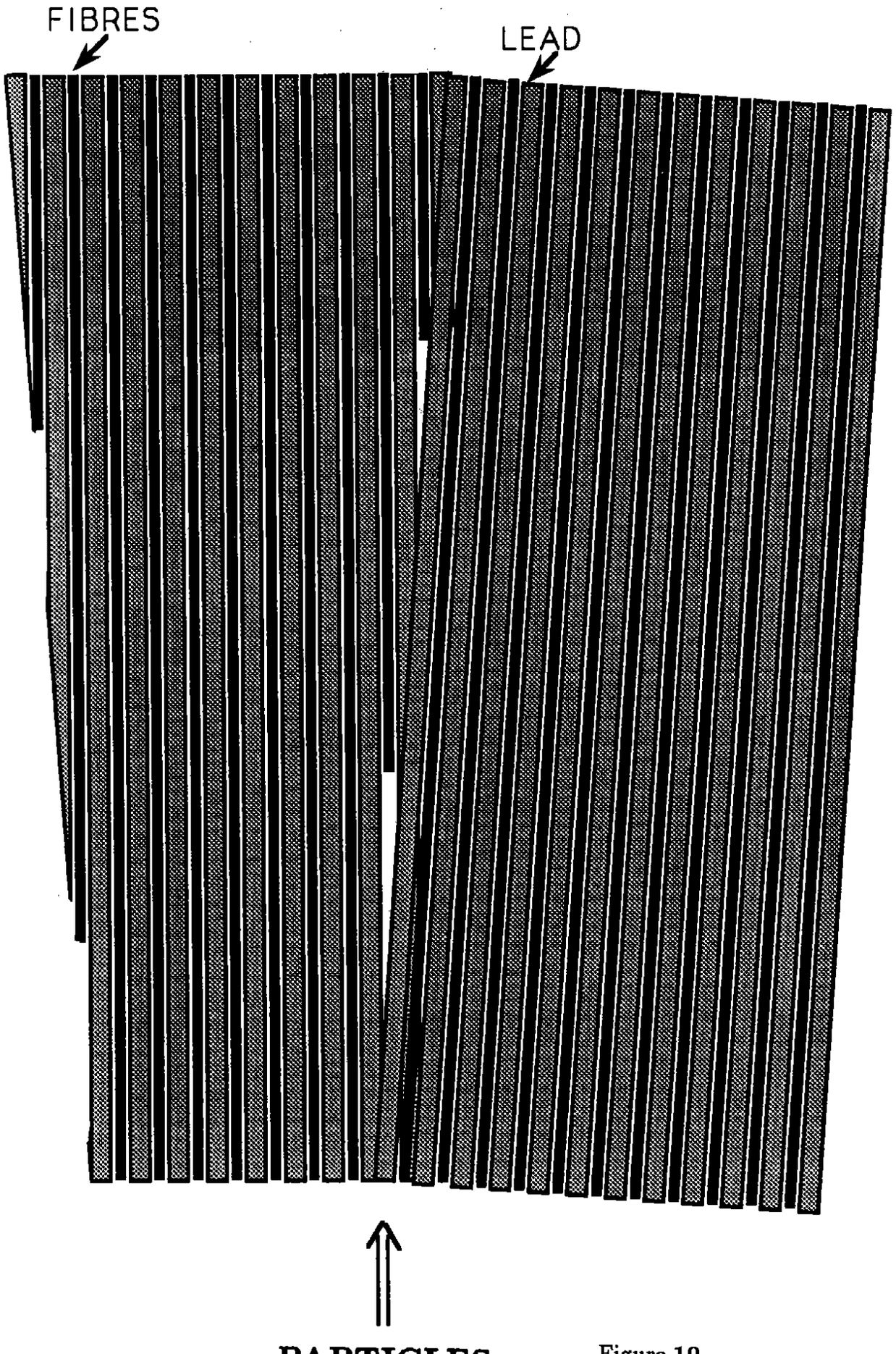


Figure 10

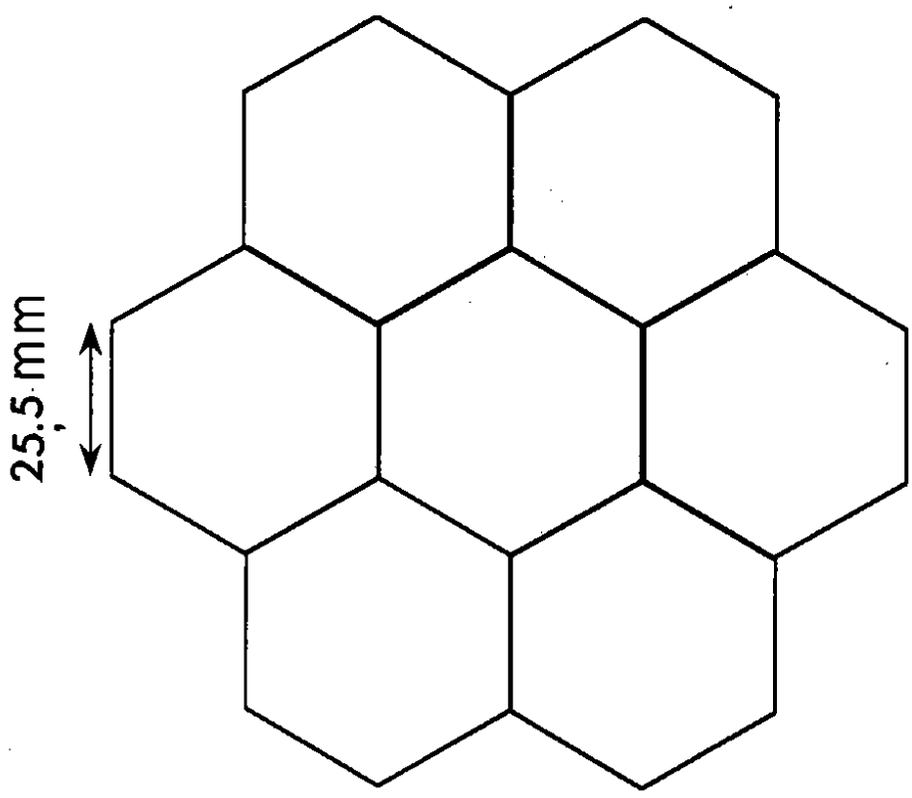


Figure 11

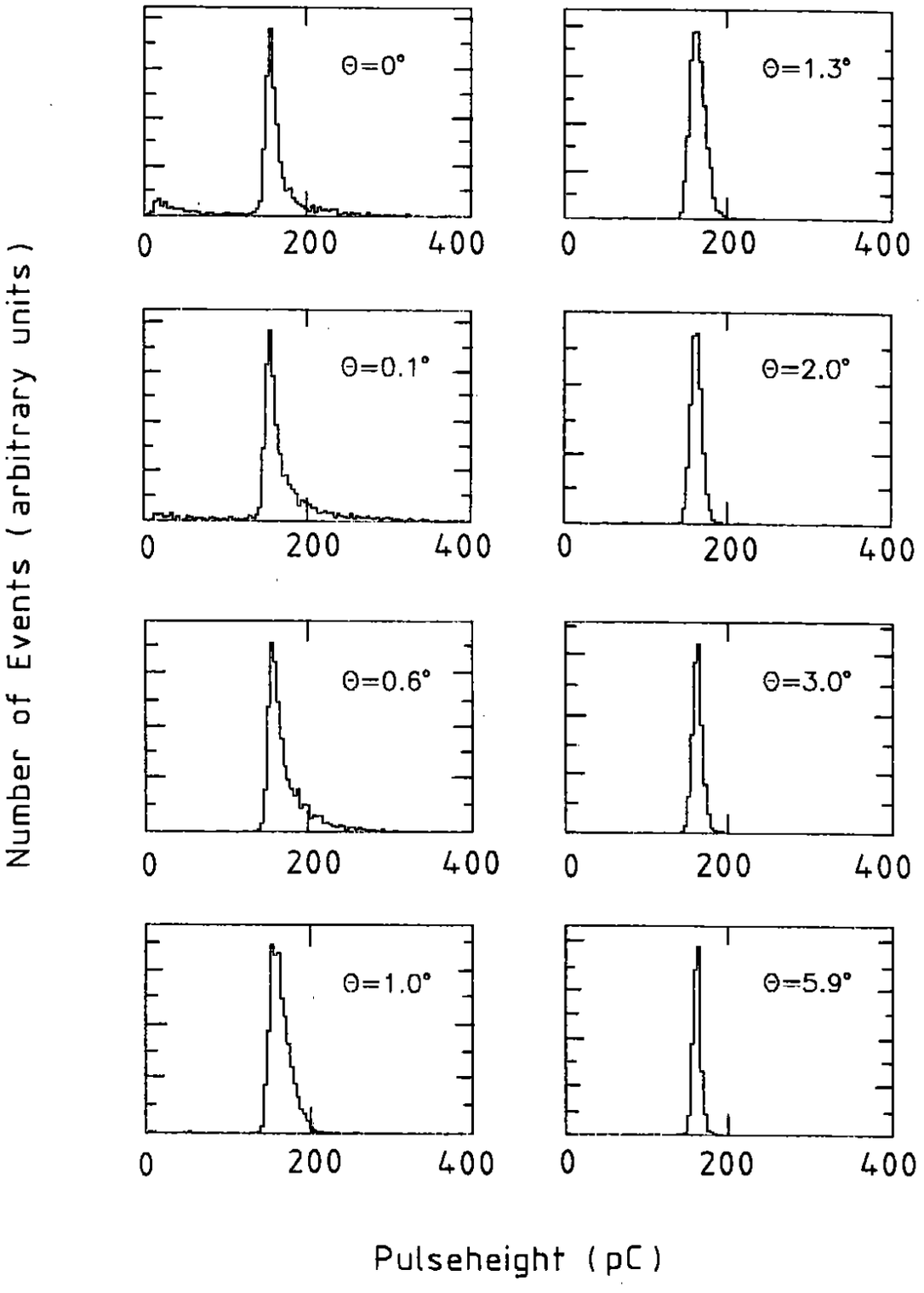
Θ=0°
Θ=1.3°
Θ=0.1°
Θ=2.0°
Θ=0.6°
Θ=3.0°
Θ=1.0°
Θ=5.9°
0
200
400
Number of Events ( arbitrary units )
Pulseheight ( pC )

**Figure 12**

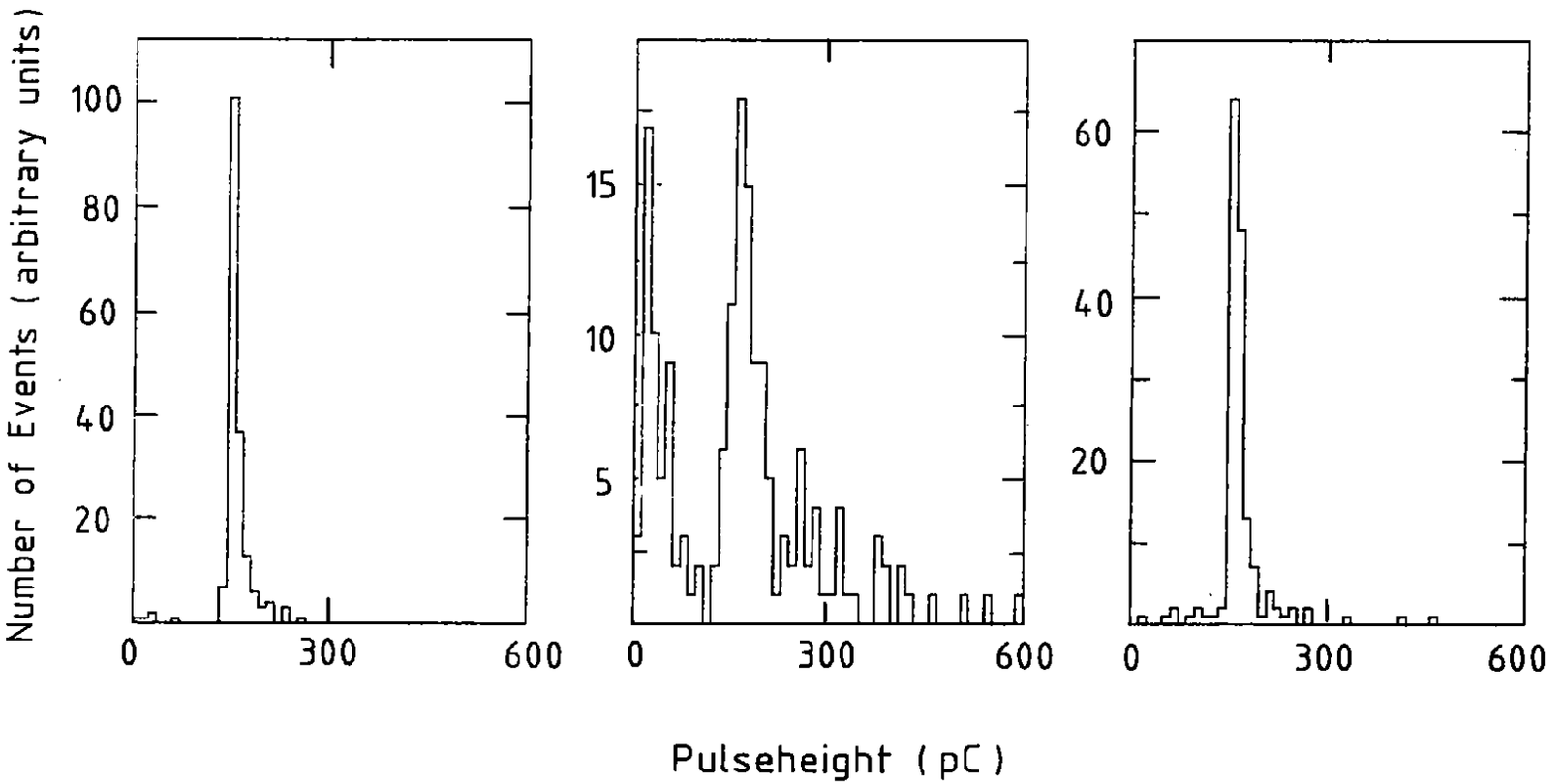
Number of Events ( arbitrary units)
100
80
60
40
20
0
300
600
15
10
5
0
300
600
60
40
20
0
300
600
Pulseheight ( pC )

Figure 13

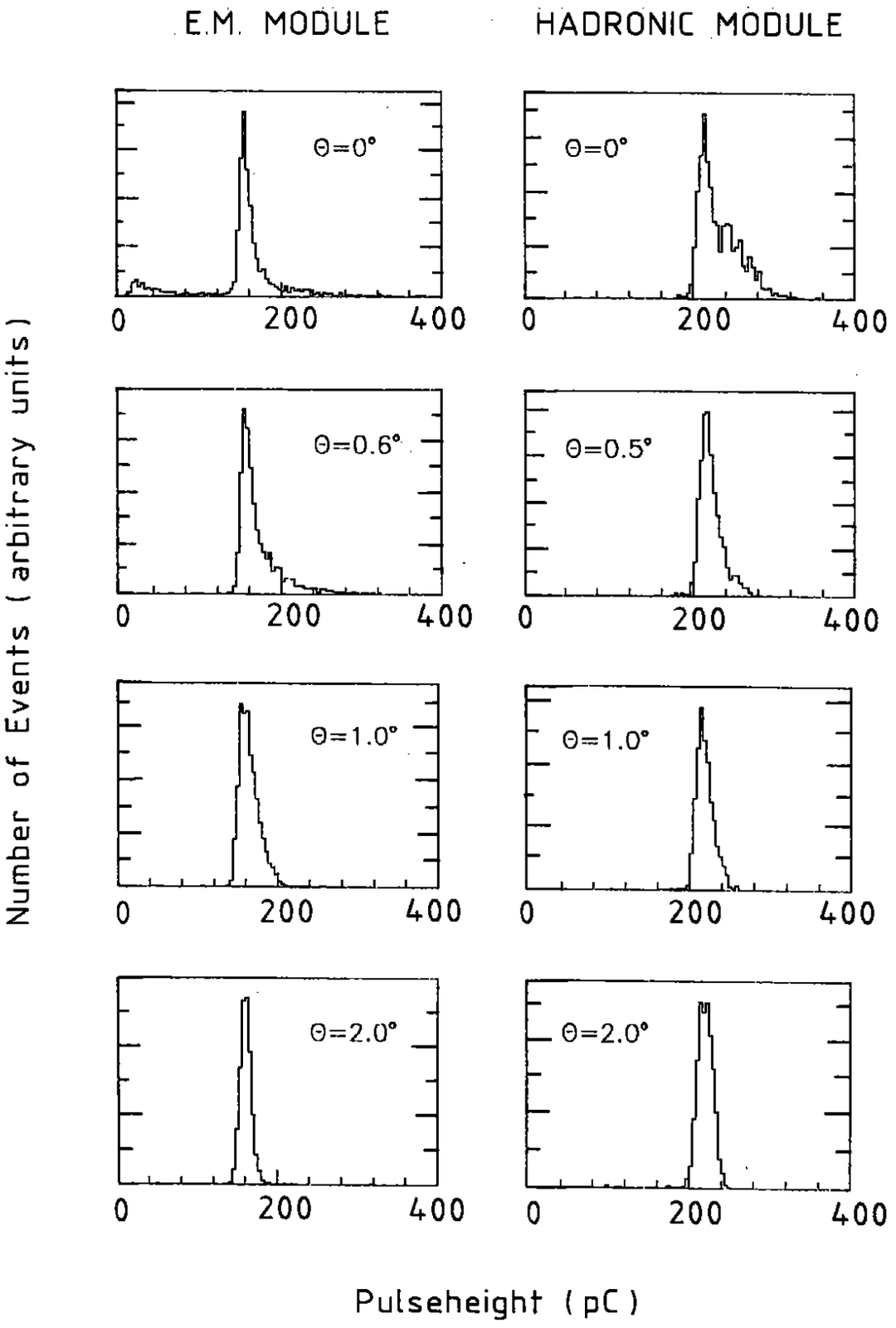
E.M. MODULE
HADRONIC MODULE
Θ=0°
Θ=0°
Θ=0.6°
Θ=0.5°
Θ=1.0°
Θ=1.0°
Θ=2.0°
Θ=2.0°
0
200
400
Number of Events ( arbitrary units )
Pulseheight ( pC )

Figure 14

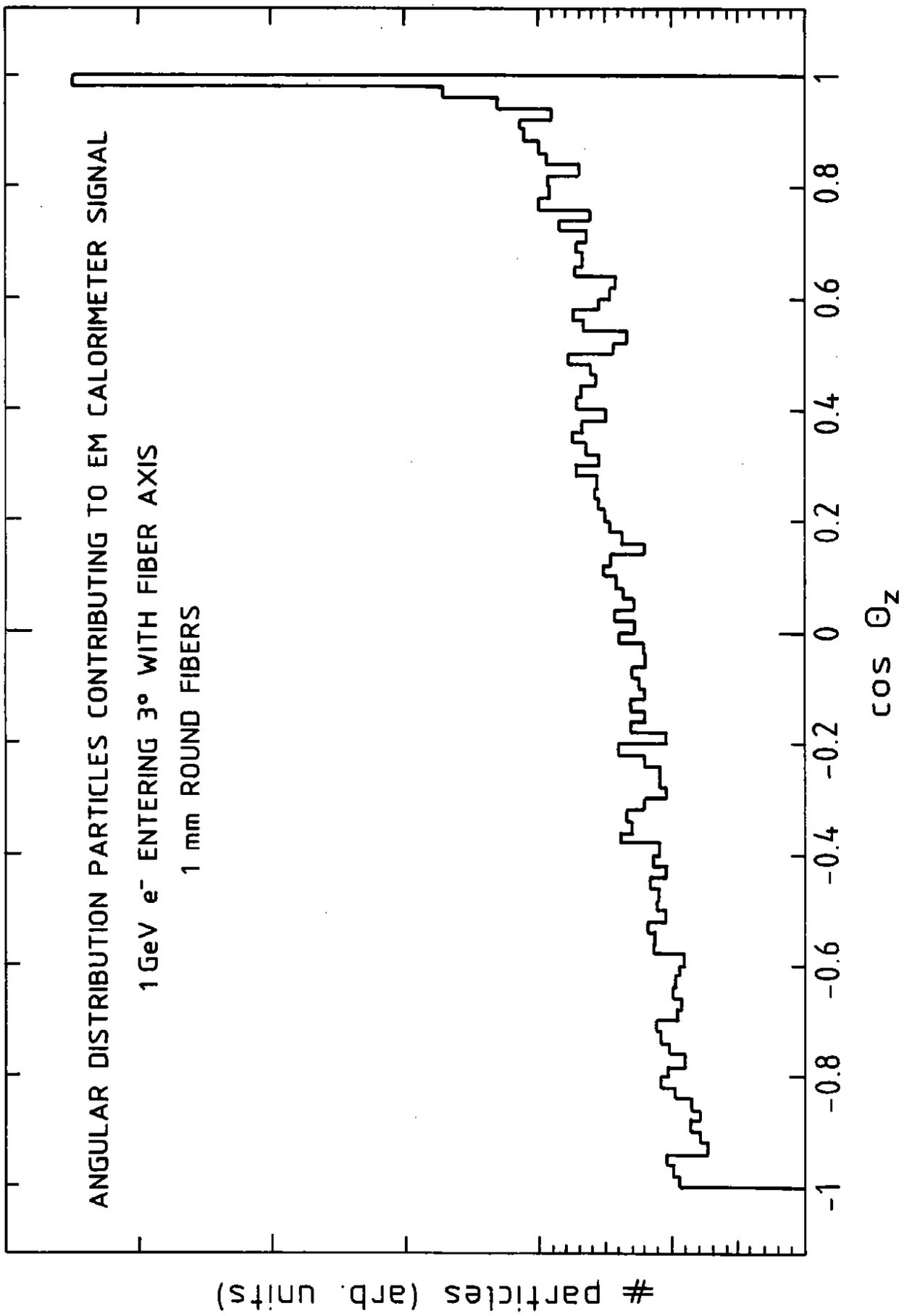
ANGULAR DISTRIBUTION PARTICLES CONTRIBUTING TO EM CALORIMETER SIGNAL
1 GeV e⁻ ENTERING 3° WITH FIBER AXIS
1 mm ROUND FIBERS
# particles (arb. units)
cos Θz
-1
-0.8
-0.6
-0.4
-0.2
0
0.2
0.4
0.6
0.8
1

**Figure 15**

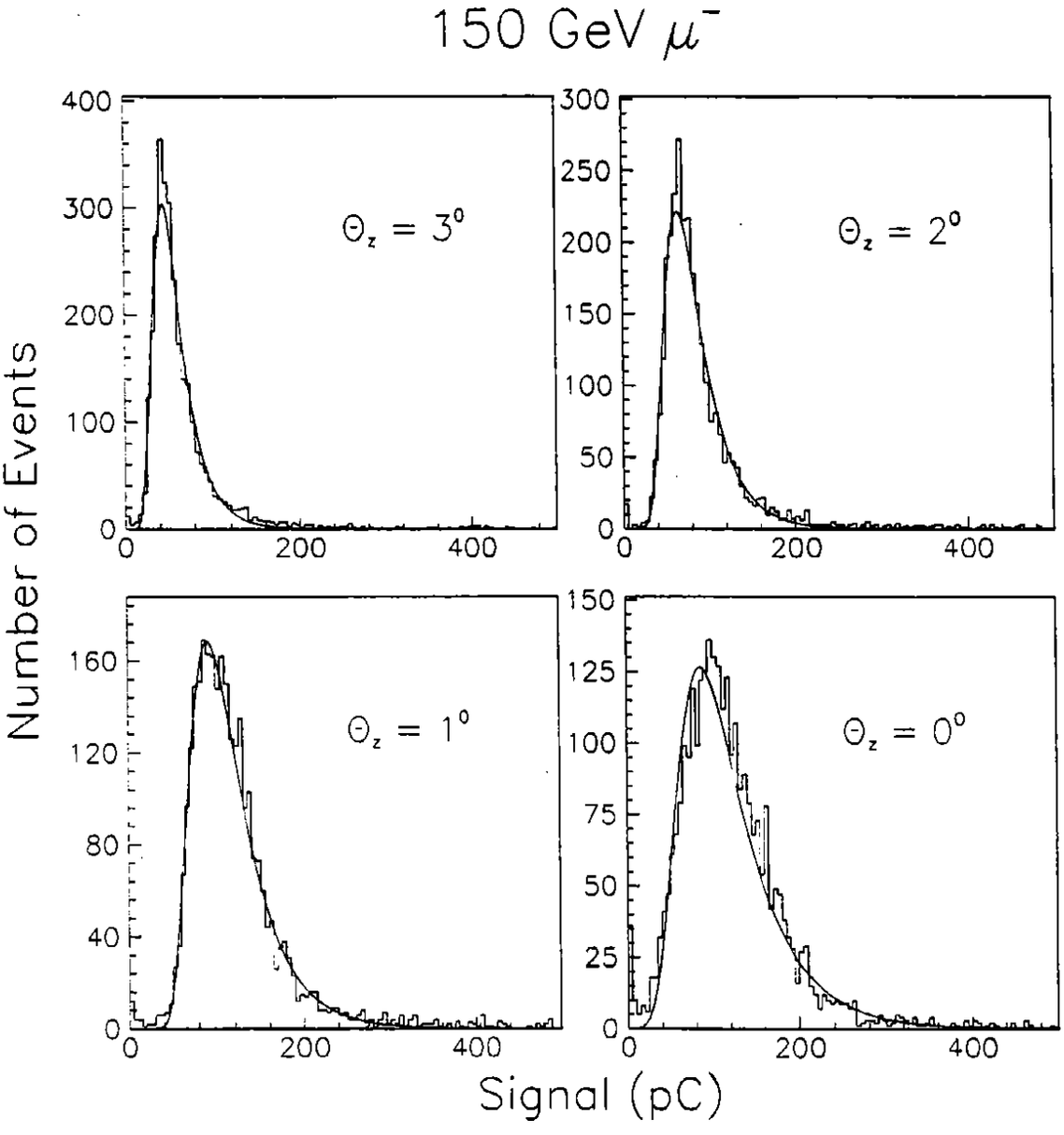
150 GeV $\mu^-$
$\Theta_z = 3^0$
$\Theta_z = 2^0$
$\Theta_z = 1^0$
$\Theta_z = 0^0$
Number of Events
Signal (pC)

**Figure 16**

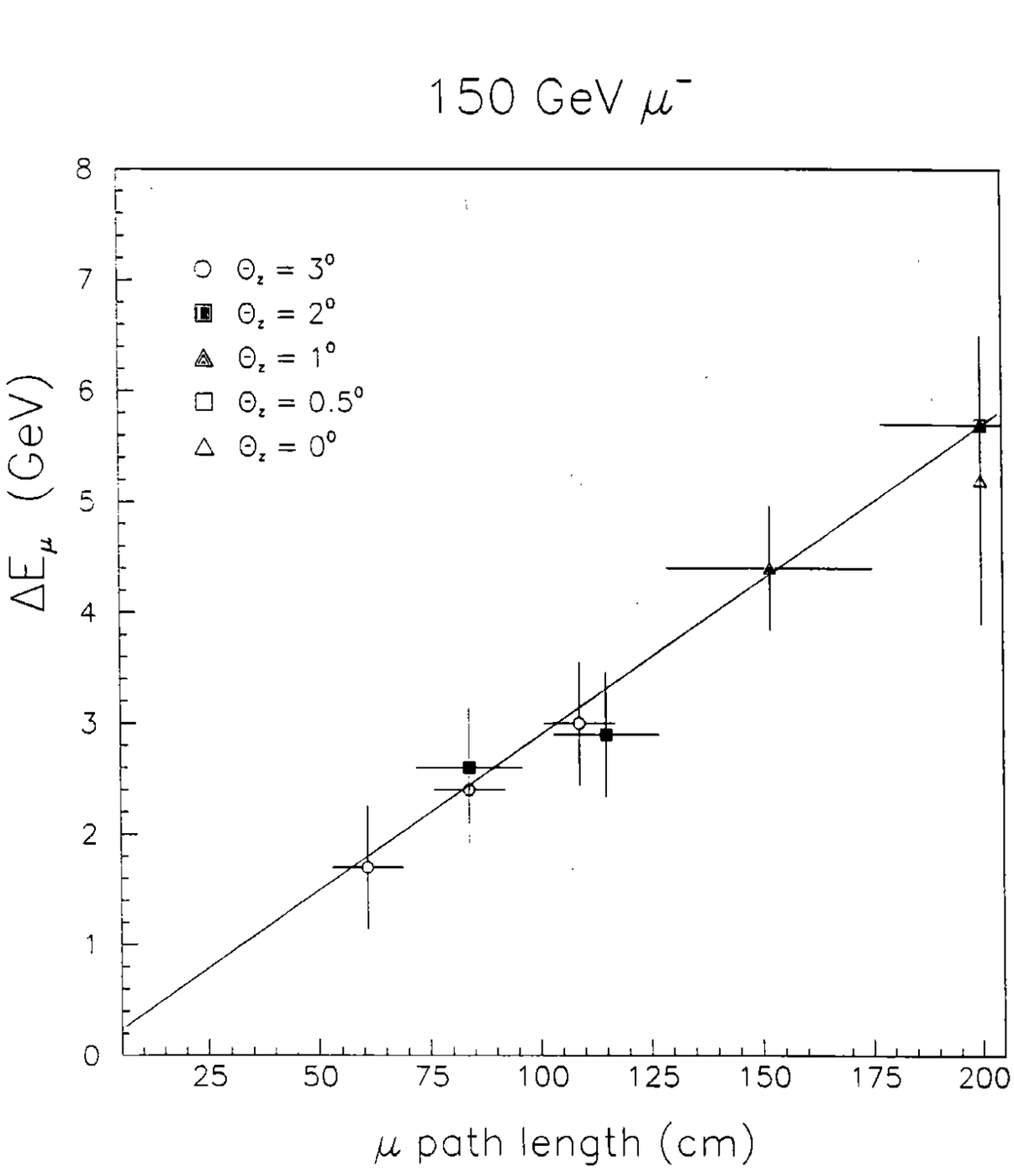
150 GeV $\mu^-$
$\Theta_z = 3°$
$\Theta_z = 2°$
$\Theta_z = 1°$
$\Theta_z = 0.5°$
$\Theta_z = 0°$
$\Delta E_\mu$ (GeV)
$\mu$ path length (cm)
0
1
2
3
4
5
6
7
8
25
50
75
100
125
150
175
200

**Figure 17**

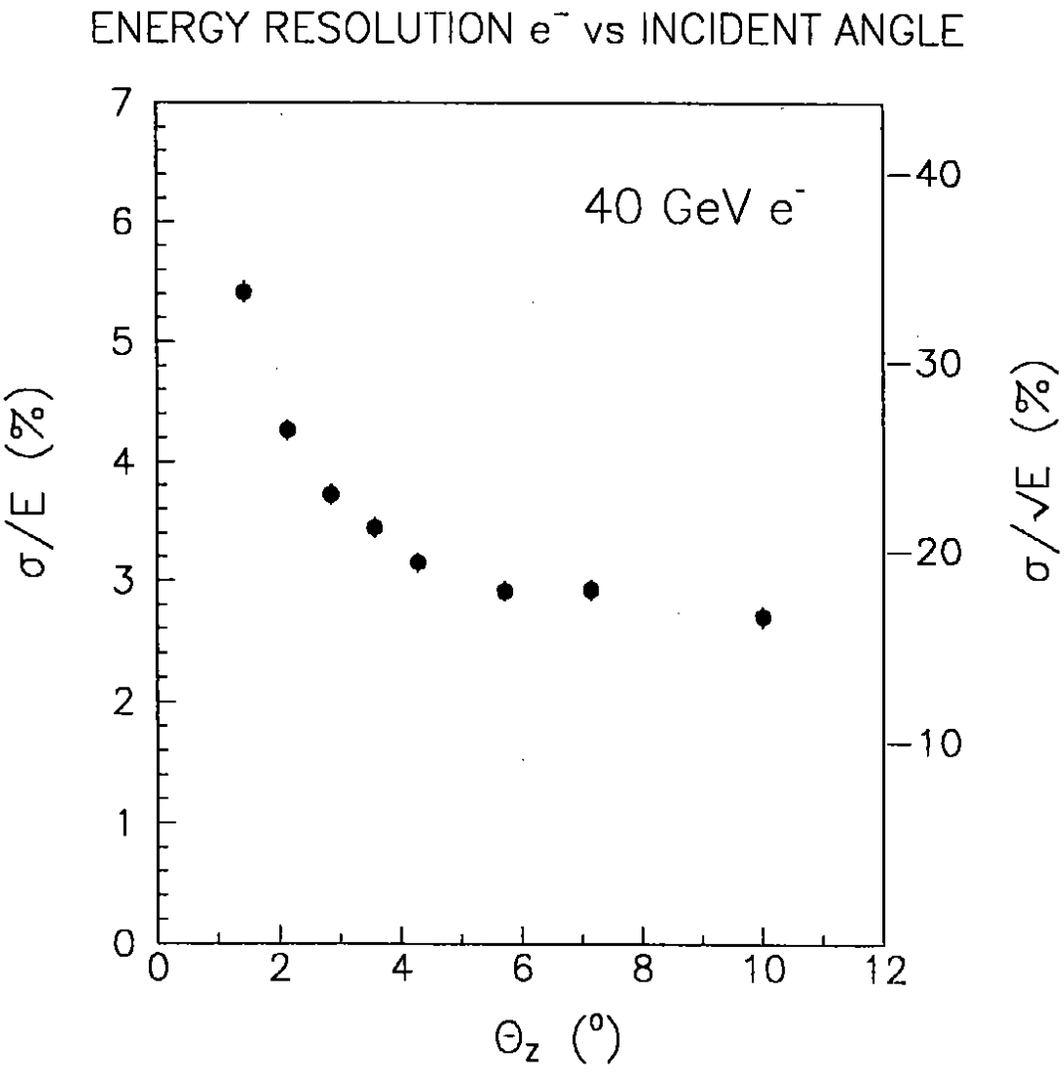
ENERGY RESOLUTION e⁻ vs INCIDENT ANGLE
40 GeV e⁻
σ/E (%)
σ/√E (%)
Θz (°)
0
1
2
3
4
5
6
7
0
2
4
6
8
10
12
10
20
30
40

**Figure 18**

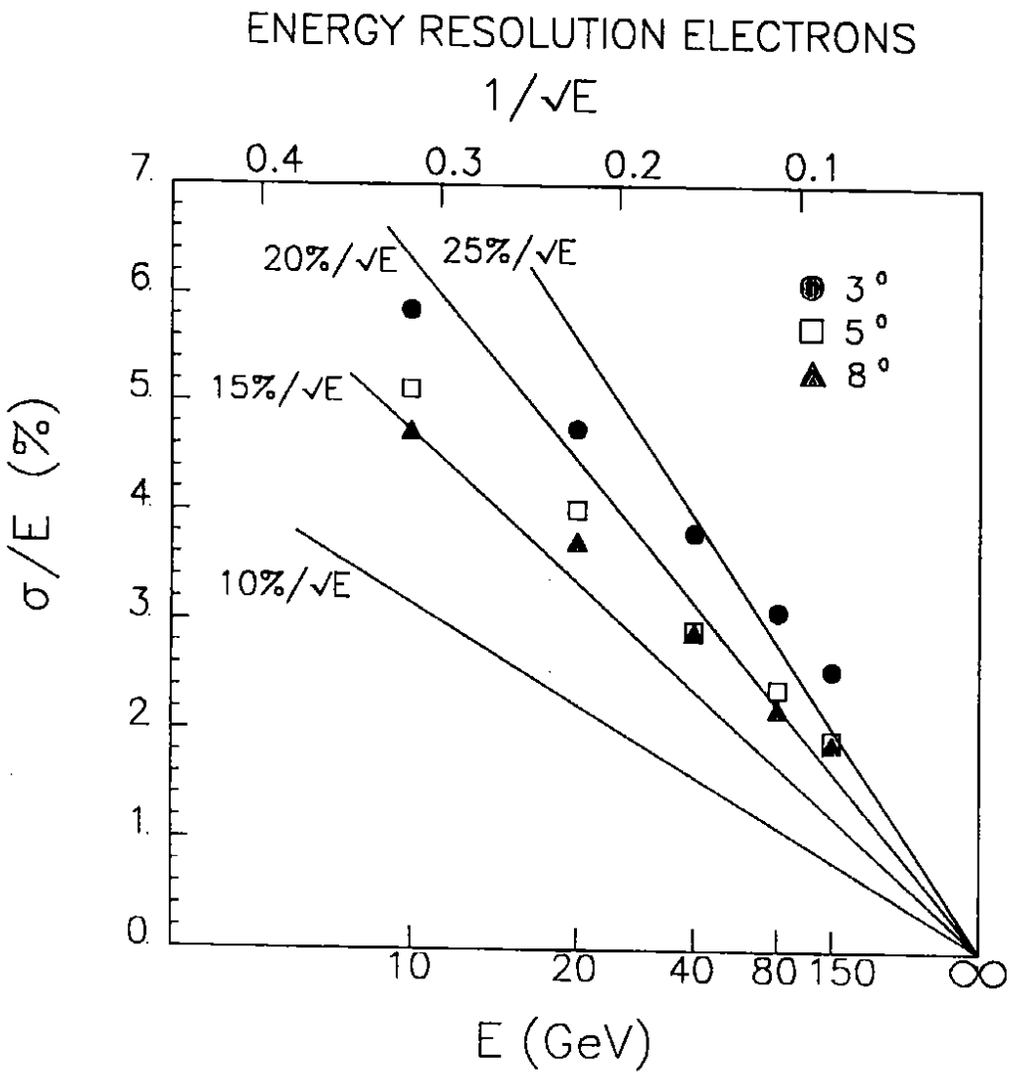
ENERGY RESOLUTION ELECTRONS
1/√E
0.4
0.3
0.2
0.1
7.
6.
5.
4.
3.
2.
1.
0.
σ/E (%)
20%/√E
25%/√E
15%/√E
10%/√E
3°
5°
8°
10
20
40
80
150
∞
E (GeV)

**Figure 19**

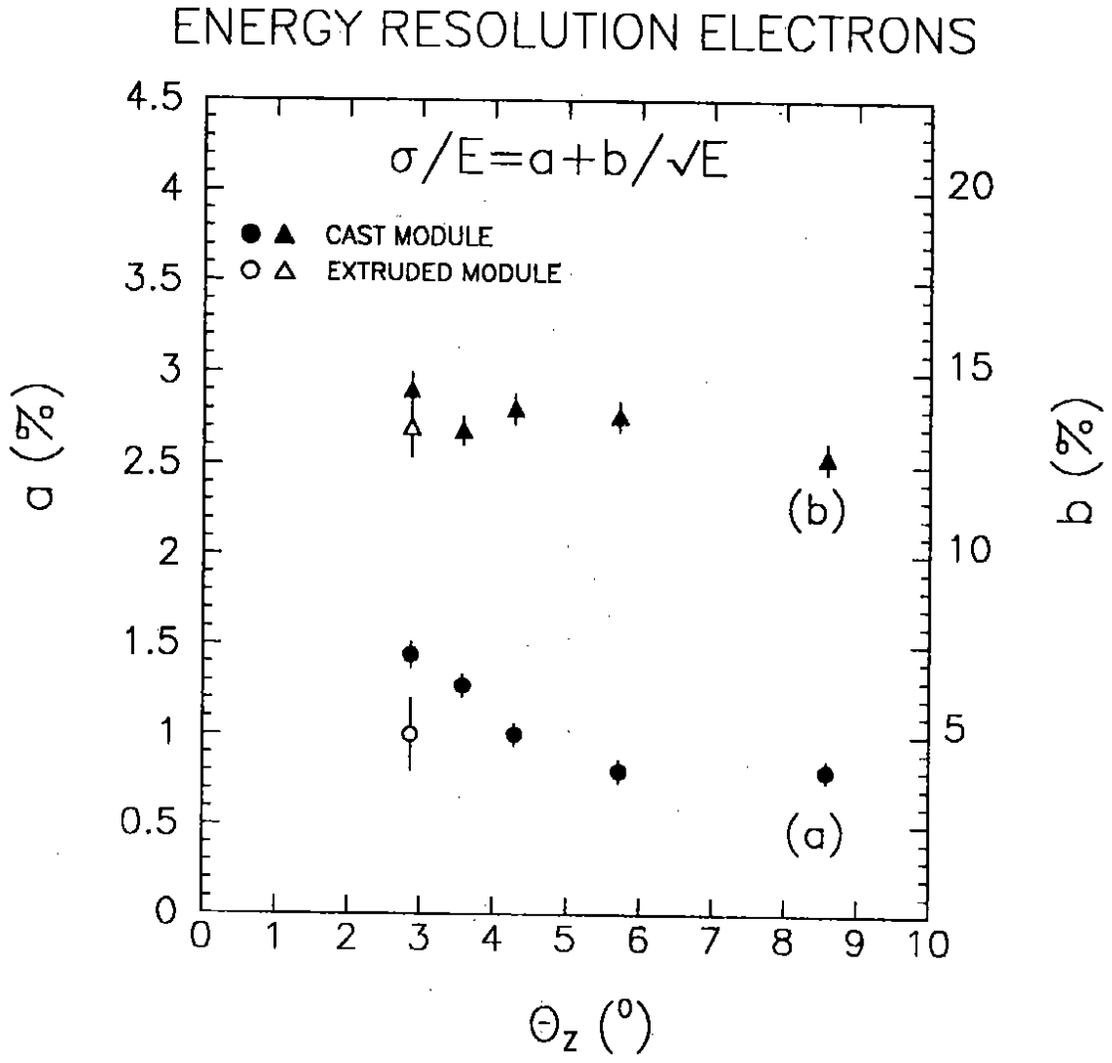
ENERGY RESOLUTION ELECTRONS
σ/E=a+b/√E
CAST MODULE
EXTRUDED MODULE
(a)
(b)
a (%)
b (%)
Θz (°)
4.5
4
3.5
3
2.5
2
1.5
1
0.5
0
20
15
10
5
0 1 2 3 4 5 6 7 8 9 10

**Figure 20**

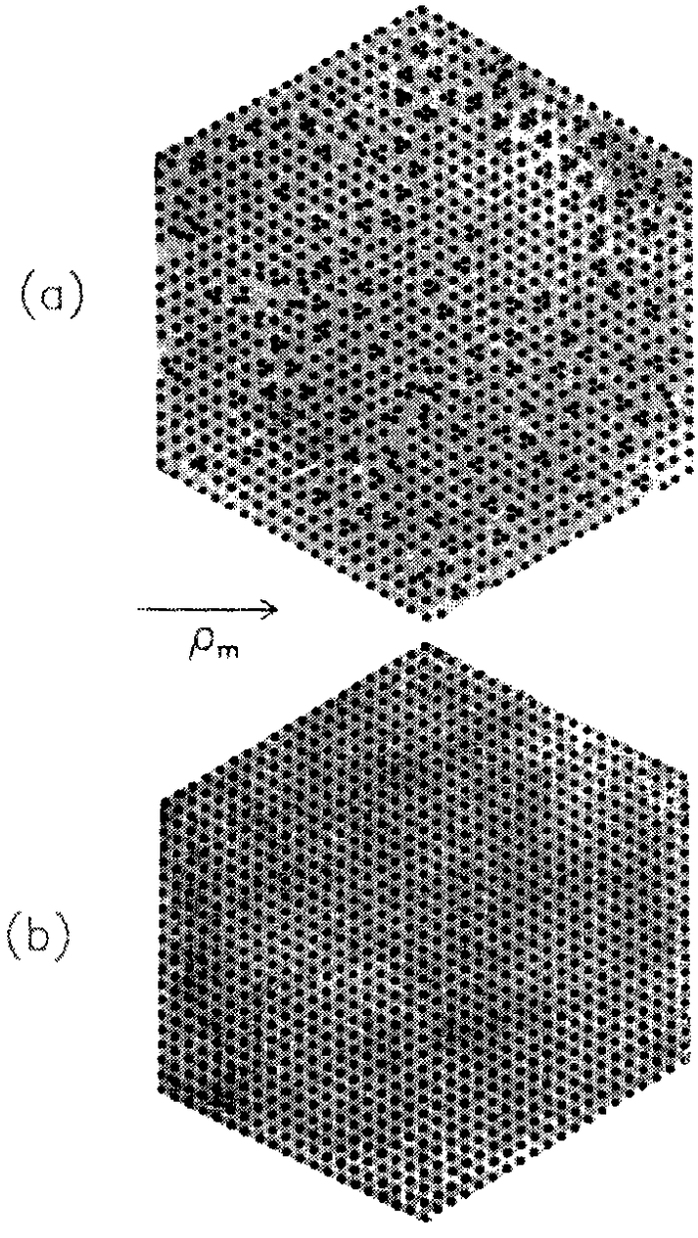


**Figure 21**

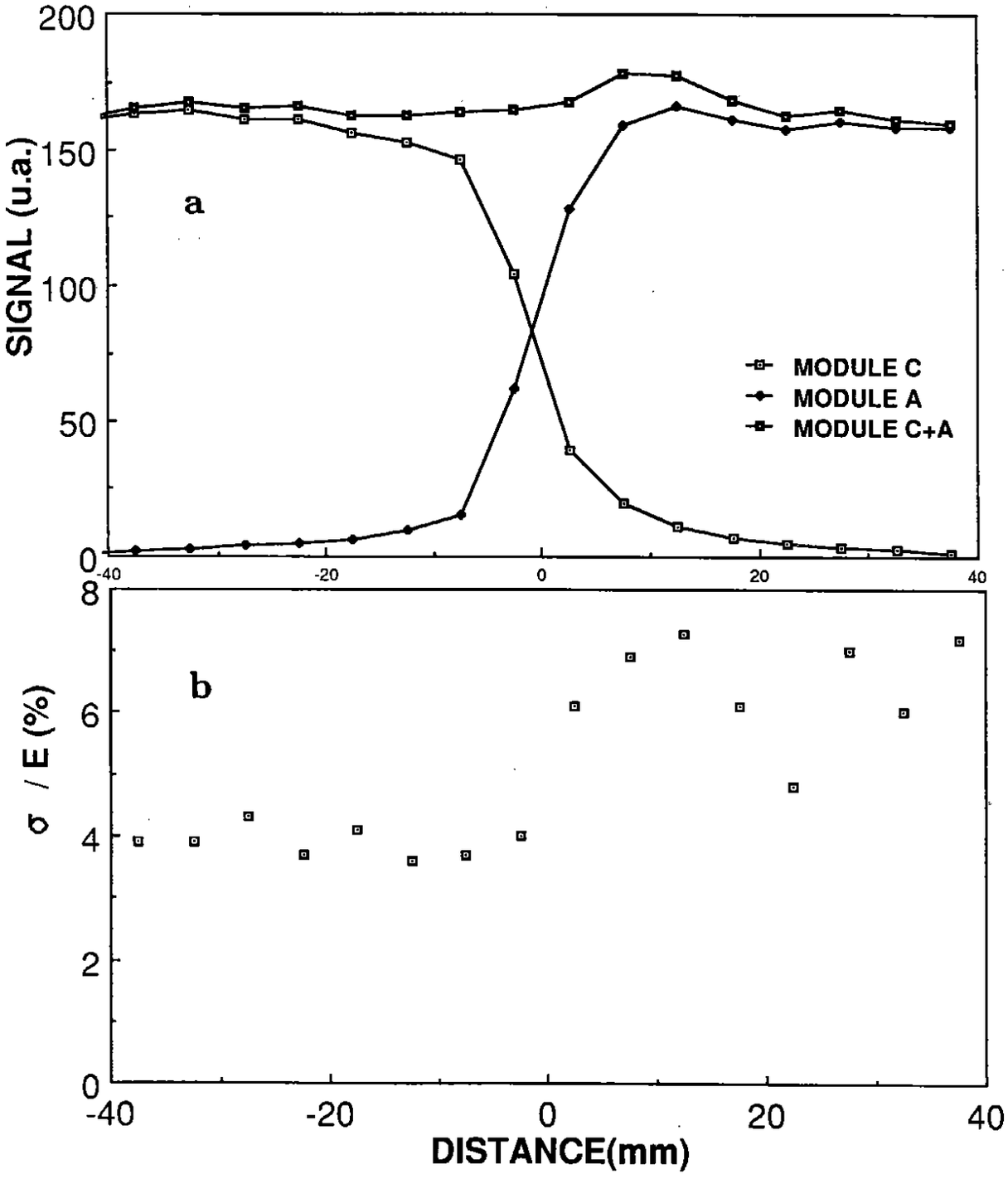
200
150
100
50
0
SIGNAL (u.a.)
a
MODULE C
MODULE A
MODULE C+A
-40
-20
0
20
40
8
6
4
2
0
σ / E (%)
b
-40
-20
0
20
40
DISTANCE(mm)

Figure 22

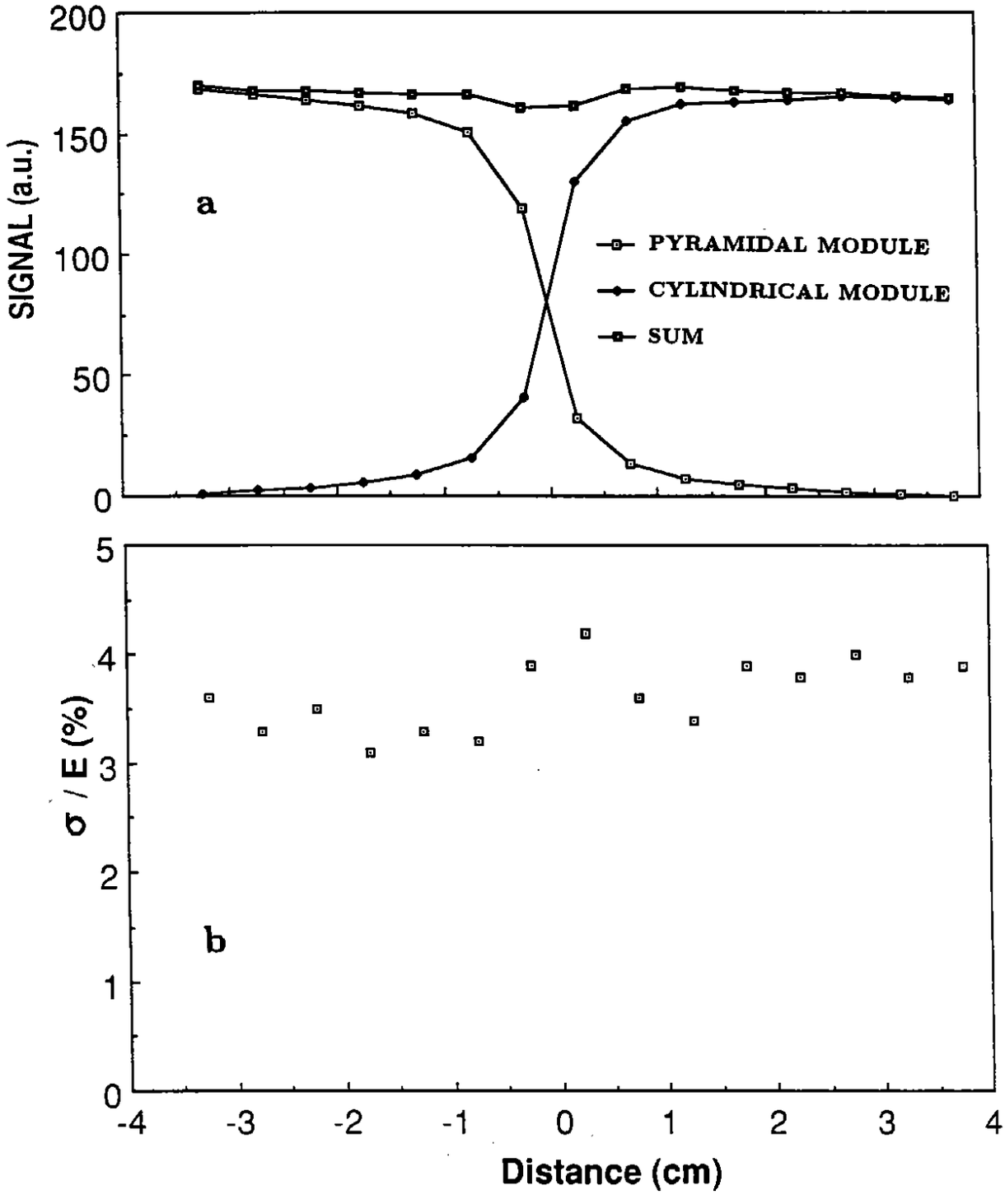
200
150
100
50
0
SIGNAL (a.u.)
a
PYRAMIDAL MODULE
CYLINDRICAL MODULE
SUM
5
4
3
2
1
0
σ / E (%)
b
-4
-3
-2
-1
0
1
2
3
4
Distance (cm)

Figure 23

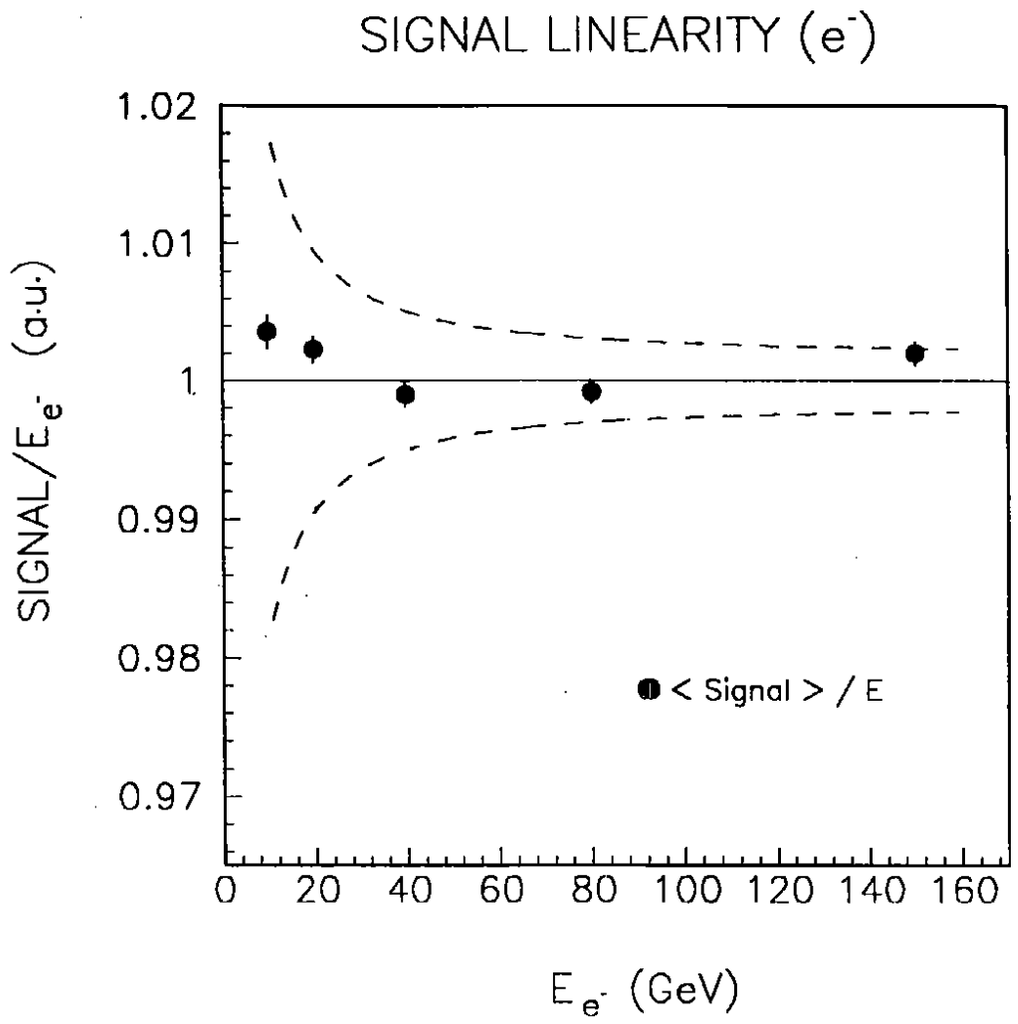
SIGNAL LINEARITY (e⁻)
1.02
1.01
1
0.99
0.98
0.97
SIGNAL/E_e⁻ (a.u.)
< Signal > / E
0
20
40
60
80
100
120
140
160
E_e⁻ (GeV)

**Figure 24**

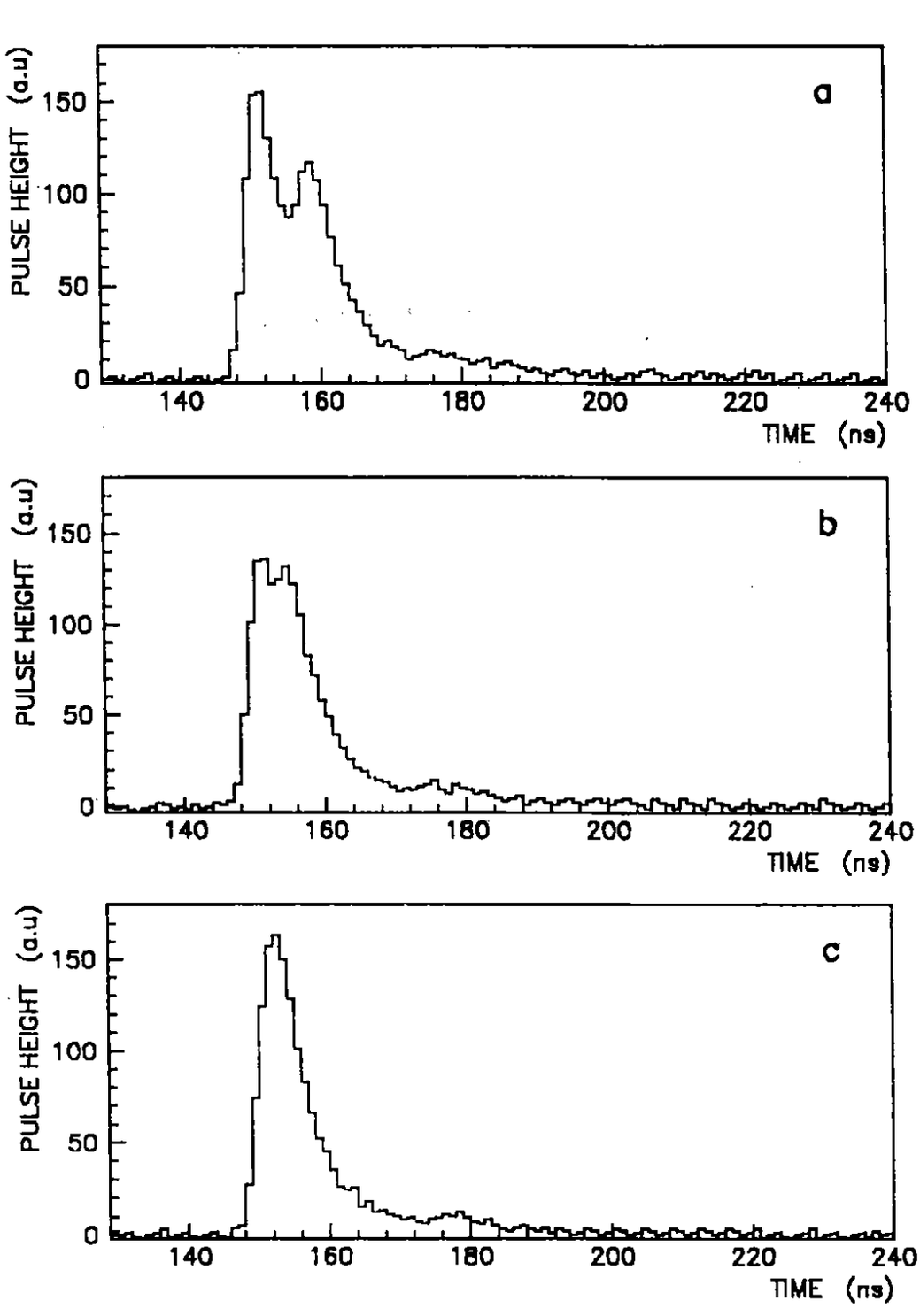


Figure 25

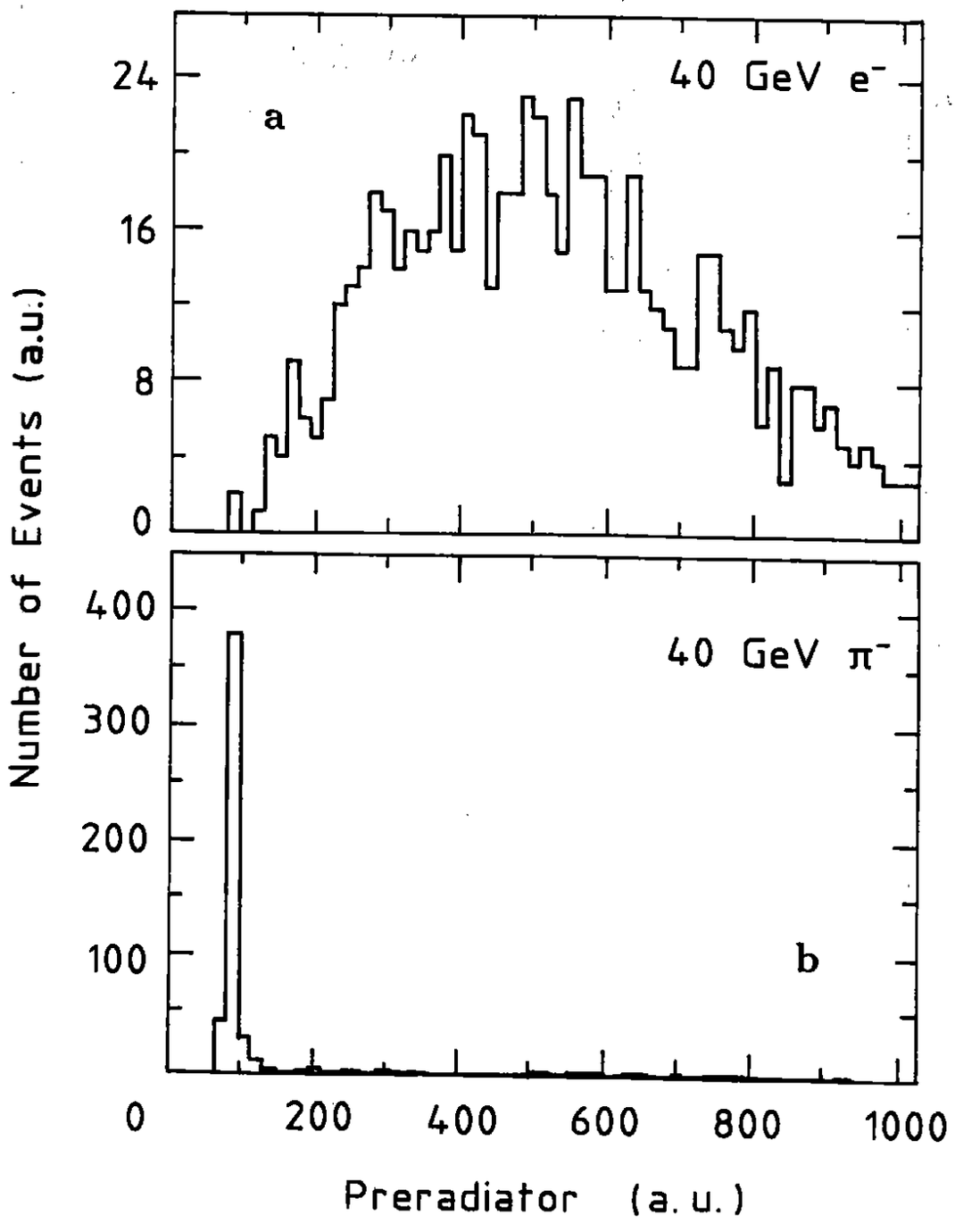
40 GeV e⁻
a
24
16
8
0
40 GeV π⁻
b
400
300
200
100
0
200
400
600
800
1000
Number of Events (a.u.)
Preradiator (a.u.)

Figure 26

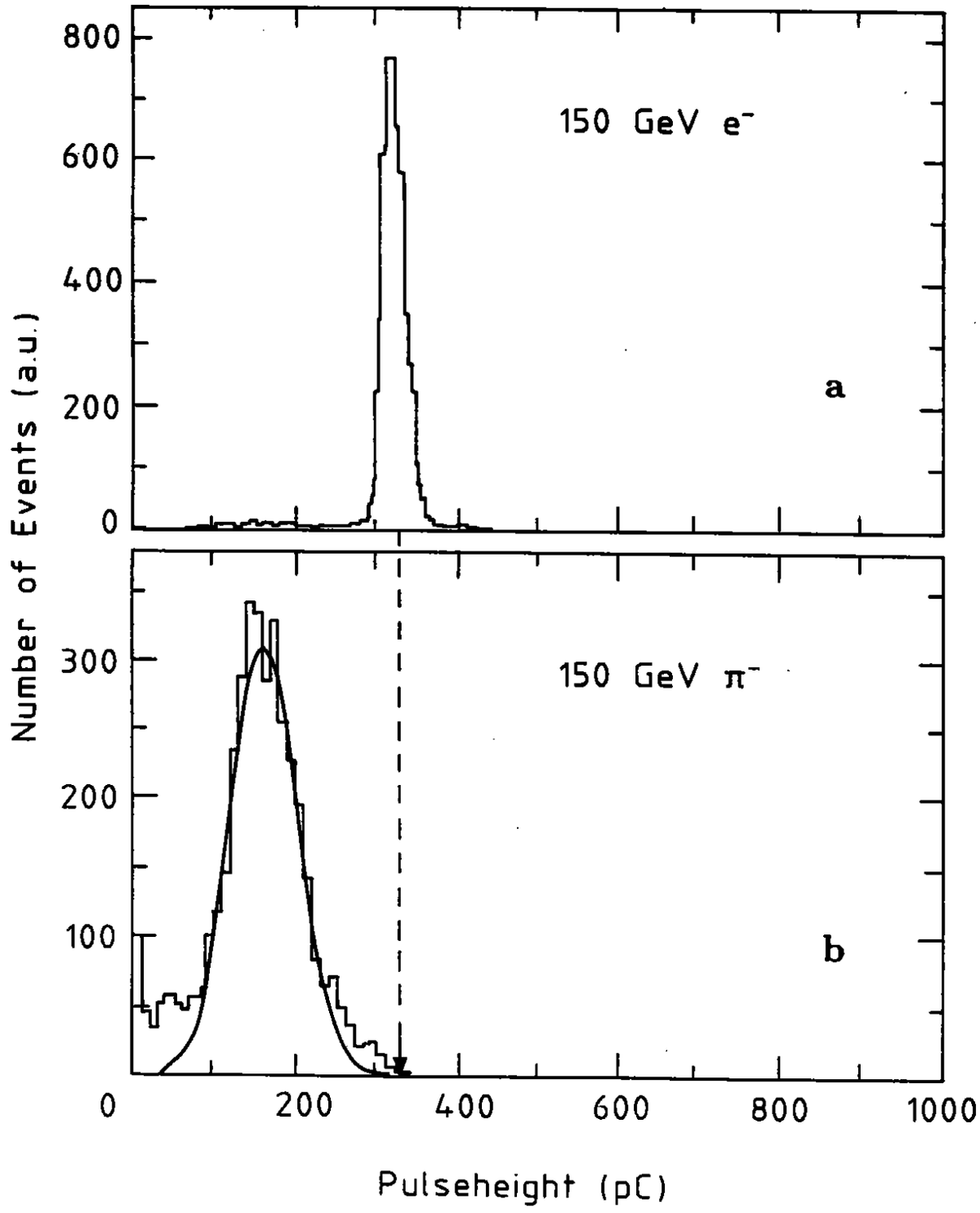
800
600
400
200
0
150 GeV e⁻
a
300
200
100
150 GeV π⁻
b
Number of Events (a.u.)
0
200
400
600
800
1000
Pulseheight (pC)

Figure 27

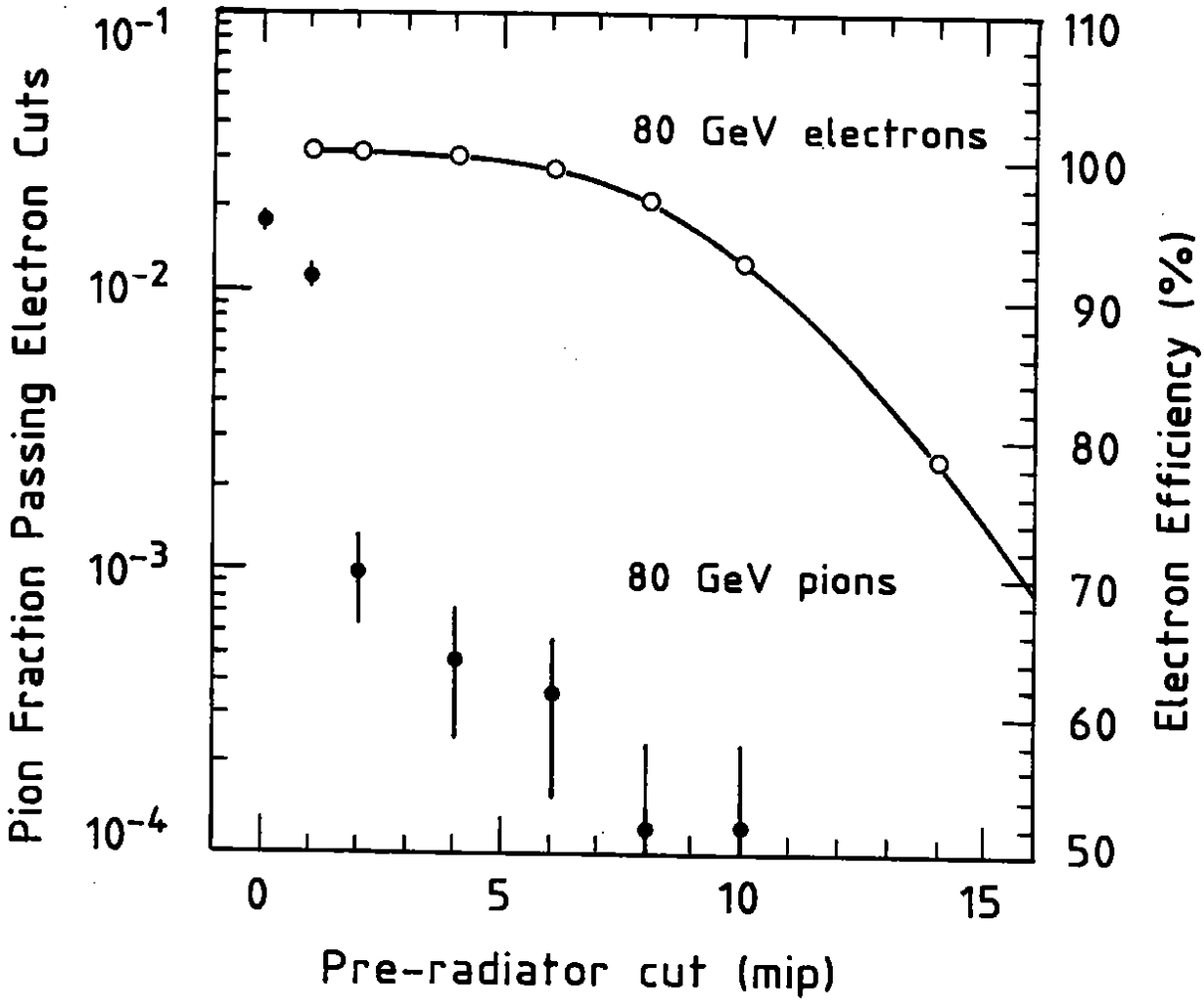
Pion Fraction Passing Electron Cuts
$10^{-1}$
$10^{-2}$
$10^{-3}$
$10^{-4}$
80 GeV electrons
80 GeV pions
0
5
10
15
Pre-radiator cut (mip)
110
100
90
80
70
60
50
Electron Efficiency (%)

Figure 28